

# DISSERTATION

## **Focused Ion Beam Induced Synthesis of Nanowires**

ausgeführt zum Zwecke der Erlangung des akademischen Grades  
eines Doktors der technischen Wissenschaften von

**Dipl.-Ing. Christoph Schöndorfer**

Matr.-Nr. 9625000

Stöcklfeld 2

4786 Brunnenthal

an der Technischen Universität Wien  
Fakultät für Elektrotechnik und Informationstechnik  
Institut für Festkörperelektronik, E362

unter der Leitung von

**O. Univ.-Prof. Dr. Emmerich Bertagnolli**

Wien, im Juni 2008

.....

I declare in the lieu of oath that I did this dissertation in hand by myself using only literature cited at the end of this volume.

Vienna, June 2008

.....

# Abstract

The ongoing process of shrinking dimensions for future nanoscale devices and on-chip applications is expected to greatly increase the performances. Due to the essential need of new fabrication methods low-dimensional nanostructures such as thin films (2-D), nanotubes and nanowires (1-D) and quantum dots (0-D) are required. For 1-D nanofabrication, two different approaches can be followed, the so-called “top-down” and the “bottom-up” approach. With the former approach, the nanostructures are generated by etching the substrate usually using lithographically processed masks. This method is very time-consuming as a lot of experiments have to be carried out to obtain the desired results. With the latter approach, nanowires are grown from the bottom-up on a substrate, e.g. by the vapor-liquid-solid (VLS) growth mechanism in combination with a metal catalyst or the electrochemical deposition (ECD) using templates such as anodic alumina membranes.

The present work focusses on the investigation of a novel gallium focused ion beam (FIB) based approach for synthesis of nanowires on germanium, gallium antimonide and in particular on pure antimony substrates. In contrast to the above-mentioned techniques this process offers a new possibility of nanostructure formation in a completely different way as no external temperature treatment nor any additional material source is needed.

The FIB stimulated nanowire growth is discussed based on a model similar to VLS with gallium acting as catalyst. Thereby, a catalytic metal particle on the sample surface forms a liquid alloy cluster if the ambient temperature is high enough and serves as the preferential site for adsorption of reactant from the vapor phase. It is supposed that supersaturation is the driving force for nucleation of seeds at the interface between the alloy cluster and the substrate surface giving rise to a highly anisotropic growth of nanostructures. It is assumed that FIB processing produces mobile Ga species on the surface, which rapidly agglomerate forming catalytic nanoclusters. Sputtered Sb diffuses on the surface and acts as a quasi-vapor phase source. When the dissolved Sb concentration exceeds solubility, nucleation sites will be formed which initiate the precipitation of the Sb. Nanowire growth continues as long as the droplet remains in a liquid state and supersaturation is maintained.

Individual nanowires deposited on isolating substrates and contacted by electrodes for electrical characterization show a strong dependency on the surrounding ambient atmosphere. During measurements at room temperature a significant change of the resistance over several orders of magnitude is observed when such a nanowire device is exposed to water or ethanol vapor. The electrical behavior is unaffected by exposure to a pure oxygen, helium, hydrogen, carbon monoxide or vacuum ambient. Both, chemical selectivity and sensitivity make Sb nanowires interesting candidates for future sensor applications.

## Kurzfassung

Anwendungen aus Nanotechnologie und Nanoelektronik beeinflussen bereits jetzt das Alltagsgeschehen nachhaltig. Um noch leistungsfähigere Komponenten herstellen zu können, muss die Miniaturisierung der Strukturen weiter vorangetrieben werden. Damit man diesen Anforderungen gerecht wird, ist es allerdings notwendig, neue Herstellungsverfahren für niedrig-dimensionale Nanostrukturen wie dünne Schichten (2-D), Nanoröhrchen und Nanodrähte (1-D) und Quantenpunkte (0-D) zu etablieren. Für die Erzeugung von 1-D-Nanostrukturen gibt es im Wesentlichen zwei Möglichkeiten, den “Top-Down”-Prozess und den “Bottom-Up”-Prozess. Beim “Top-Down”-Prozess werden die Proben mit geeigneten Masken versehen und anschließend die entsprechenden Strukturen aus dem Substrat herausgeätzt. Dieses Verfahren ist jedoch sehr aufwendig, es erfordert in der Regel eine Vielzahl an Vorlaufexperimenten um die gewünschten Strukturen zu erhalten. Beim “Bottom-Up”-Prozess hingegen werden die Nanostrukturen auf dem Substrat aufgewachsen. Stellvertretend für eine Vielzahl an Verfahren seien hier der “Vapor-Liquid-Solid”-Wachstumsmechanismus (VLS), ein katalytischer Prozess in Verbindung mit einem Metallpartikel und die elektrochemische Deposition (ECD), bei der Material auf einer vorstrukturierten Membran abgeschieden wird, angeführt.

Die vorliegende Arbeit beschäftigt sich mit einer neuen Methode zur Synthese von Germanium-, Galliumantimonid- und im Speziellen von Antimon-Nanodrähten durch den Einsatz eines fokussierten Gallium-Ionenstrahls (FIB, von engl. “focused ion beam”). Im Gegensatz zu den bereits erwähnten Verfahren ist hier weder die Zufuhr von Temperatur noch eine zusätzliche Materialquelle erforderlich.

Zur Diskussion dieses FIB-induzierten Wachstums von Nanodrähten wird ein Modell ähnlich dem des VLS-Wachstumsprozesses mit Gallium als Katalysator herangezogen. Dabei dient ein metallisches Partikel auf der Substratoberfläche, das bei hinreichend hoher Umgebungstemperatur einen katalytisch aktiven Nanotropfen bildet, als bevorzugte Stelle für die Adsorption eines gasförmig zugeführten Reaktants. Im Falle einer Übersättigung des gelösten Materials kommt es zur Nukleation eines Keims an der Grenzfläche zwischen dem Substrat und dem Nanotropfen, was letztendlich zu einem anisotropen Wachstum von Nanodrähten führt. Es wird vermutet, dass beim FIB-Prozess

an der Substratoberfläche eine hochmobile Gallium-Spezies erzeugt wird, die rasch zu flüssigen, katalytisch aktiven Nanotropfen agglomeriert. Gesputtertes Antimon wiederum kann an der Oberfläche diffundieren, sich in diesen Nanotropfen lösen und daher als die benötigte Materialquelle fungieren. Wenn die Antimon-Konzentration die maximale Löslichkeit übersteigt, scheidet sich Antimon in Form von Nanodrähten aus. Solange der Katalysator flüssig bleibt und die Übersättigung durch permanenten Nachschub gewährleistet ist, kann der Nanodraht weiterwachsen.

Einzelne Nanodrähte werden auf Substrate übertragen, die mit einer isolierenden Schicht überzogen sind, und im Anschluss mit Metallelektroden versehen. Die nachfolgende elektrische Charakterisierung zeigt eine starke Abhängigkeit der Messergebnisse von der Atmosphäre, die die Probe umgibt. Eine signifikante Veränderung des Widerstands über mehrere Größenordnungen kann beobachtet werden, wenn diese Antimon-Nanodrähte Wasser- oder Ethanol Dampf ausgesetzt sind. Beim Einsatz von Sauerstoff, Helium, Wasserstoff oder Kohlenmonoxid hingegen und auch bei Messungen unter Vakuumbedingungen bleiben die elektrischen Eigenschaften unverändert. Ihre Selektivität und Sensitivität machen Antimon-Nanodrähte äußerst interessant für zukünftige Anwendungen in der Sensorik.

# Acknowledgement

This thesis would not have been possible unless the support of a lot of people. Therefore, I would like to thank:

Univ.-Prof. Dr. Emmerich Bertagnolli for giving me the opportunity to do this work at the Institute of Solid State Electronics and for reviewing this thesis.

Dr. Alois Lugstein for the scientific support and for supervising my work. He has provided assistance in numerous ways.

Univ.-Prof. Dr. Christoph Eisenmenger-Sittner for reviewing this thesis and for scientific support in recent years.

All the members of my team:

Mathias Steinmair for being an excellent team-mate and friend, Andreas Steiger-Thirsfeld for assistance with the FIB system, Julia Hyun for TEM investigation, Erwin Auer for presenting a new theory every day, Thomas Burchhart and Bernd Dielacher.

Dr. Stephan Abermann, my former room-mate, for inspiration by his choice of background music and of course for the scientific support as well as Dr. Heinz Wanzenböck, Markus Fischer, Gottfried Hochleitner, Ole Bethge, and Christoph Henkel.

Univ.-Prof. Dr. Peter Pongratz, Institute of Solid State Physics and Dr. Johannes Bernardi, USTEM for advanced TEM analysis.

Dr. Philipp Nellen and Dr. Victor Callegari, EMPA Dübendorf, Switzerland for low temperature FIB processing.

Dr. Lothar Bischof, Research Center Dresden-Rossendorf, Germany for FIB processing at high temperatures and with Au and Si ion sources.

Dr. Andreas Kolitsch for giving me the opportunity to spend a few days at the Research Center Dresden-Rossendorf, Germany.

In addition to that, I would like to thank Samuel Hoffmann, EMPA Thun, Switzerland, one of my colleagues within our transnational project for his interesting ideas and the discussions.

Of course, I would like to thank all my colleagues at the Institute of Solid State Electronics for their scientific support, in particular Dr. Matthias Schramböck for AFM investigation, Elvis Mujagic for RIE processing, and Michele Nobile for wire bonding.

All the attendees of our coffee breaks used for scientific and political discussions as well as for reporting breaking news in everyday life, namely Hermann Detz, Max Austerer, Stephan Schartner and all the rest of the gang.

Gianmauro Pozzovivo for kindly reminding me not to forget to mention him in this acknowledgement.

And finally, I want to thank my parents for their mental support, my brother Sebastian for preparing some of the illustrations used in this thesis, little Sophie for making me smile at the weekends and especially Maria for giving me strength to go on when things went worse. Thank you so much!



# Contents

<b>1</b>	<b>Introduction</b>	<b>10</b>
<b>2</b>	<b>Focused Ion Beam System</b>	<b>12</b>
2.1	FIB Technique . . . . .	12
2.1.1	Ion Column and Ion Source . . . . .	15
2.1.2	Vacuum Chamber . . . . .	16
2.1.3	Gas Injection System . . . . .	16
2.2	FIB Processing . . . . .	17
2.3	Beam Scanning Strategy . . . . .	18
<b>3</b>	<b>FIB Induced Surface Evolution</b>	<b>21</b>
3.1	FIB Response of GaAs . . . . .	21
3.2	FIB Response of InAs . . . . .	23
3.3	FIB Response of Ge . . . . .	25
3.4	FIB Response of GaSb . . . . .	27
3.5	FIB Response of Sb . . . . .	31
<b>4</b>	<b>FIB induced Growth of Sb Nanowires</b>	<b>35</b>
4.1	Vertical Uplifting of a Nanowire Network on Sb . . . . .	37
4.2	Depth Profile of a FIB Milled Box on Sb . . . . .	41
4.3	TEM Analysis of Individual Sb Nanowires . . . . .	43
4.4	EDX Analysis of Sb Nanowires . . . . .	44
4.5	Raman Analysis of Sb Nanowires . . . . .	45
4.6	Mechanism of Sb Nanowire Growth . . . . .	47
4.6.1	Key Parameters for Nanowire Formation with FIB . . . . .	50
	Phase Diagram of a Binary Ga-Sb System . . . . .	50
	Formation of Catalytic Nanocluster on Sb . . . . .	51
	Impact of Substrate Temperature on the Ga-Sb System . . . . .	52
4.7	Recrystallization of Sb Nanowires . . . . .	56

---

<b>5</b>	<b>Electrical Characterization</b>	<b>59</b>
5.1	Device Fabrication and Electrical Characterization . . . . .	59
5.1.1	Contacting a Single Sb Nanowire . . . . .	59
5.2	Electrical Characterization of a Single Sb Nanowire . . . . .	62
5.3	Sensing Properties . . . . .	64
5.3.1	Sb Nanowire Response to Water Vapor . . . . .	65
5.3.2	Sb Nanowire Response to Ethanol Vapor . . . . .	67
5.4	Response and Recovery Time of the Sb Nanowire in Ethanol Vapor . . .	69
<b>6</b>	<b>Sensing Mechanism</b>	<b>71</b>
6.1	Metal Oxide based Gas Sensors . . . . .	71
6.2	Discussion of Sensing Mechanism . . . . .	73
6.2.1	Grain Boundary Barrier Modulation . . . . .	74
6.2.2	Modulation of Charge Carrier Concentration . . . . .	76
6.2.3	Conduction by Grottuss Proton Transfer Mechanism . . . . .	79
6.3	Further Criteria for Consideration . . . . .	82
	Time Dependency of Response and Recovery . . . . .	82
	Impact of Sb Nanowire Temperature . . . . .	82
	Investigation of Alternatively Processed Sb Nanostructures . . . .	84
<b>7</b>	<b>Summary and Outlook</b>	<b>85</b>
	<b>List of Own Publications</b>	<b>95</b>
	<b>List of Own Conference Contributions</b>	<b>96</b>
	<b>Curriculum Vitae</b>	<b>98</b>

# Chapter 1

## Introduction

In recent years, quasi-one-dimensional nanostructures have attracted great attention as building blocks in nanotechnology. Thereof especially semiconducting nanowires are natural candidates for a wide range of novel devices having applications in nanoelectronics [1], optoelectronics [2] and sensorics [3]. The special geometry and the unique properties of nanowires have been studied intensively because of their potential applications in fabricating gas sensors in a highly efficient manner. The detection of chemical species is central to many areas in life sciences, environmental sensing, personal safety, and national security, with economic impact in medicine, and in the automotive and aerospace industries. The basis of most electronic sensor operations is the modification of the electrical properties of an active element, due to the adsorption of molecules on the surface of the sensor material [4, 5, 6]. As nanowires show up a high surface-to-volume ratio the ambient atmosphere is crucial for the conducting behavior. Therefore they are ideal functional modules for many types of sensors [7, 8, 9].

Several techniques for the production of various types of nanowires have been reported [10, 11], such as thermal gas decomposition [12], laser ablation of powder targets [13] hot filament chemical vapor deposition [14], or supercritical fluid solution method [15]. Most of these techniques can be broadly categorized into oxide-assisted growth [16] and metal-catalyzed growth, also known as vapor-liquid-solid (VLS) growth [17]. Potential applications demand the capability of intentional positioning of nanowires. Furthermore,

electrical and optical properties strongly depend on diameter, shape and crystallographic orientation. For all these requirements VLS turned out to be the most rational and tunable growth mechanisms for the fabrication of nanometer-sized wires. However, there is still an on-going effort in developing synthesis methods with the main objective to grow nanowires at moderate temperatures in order not to damage preexisting modules.

In this work, a focused ion beam (FIB) based approach for the synthesis of nanowires at room temperature without using any additional materials source is presented [18, 19, 20]. High energy ion beams focused to diameters in the range of several tens of nanometers offer an interesting alternative to conventional lithography based pattern techniques. The ability to both, milling and deposition of material in the nanometer range turns FIB technology to a powerful tool for semiconductor-related processing. To keep up with the trend of devices to shrink in dimensions, the response of ion induced material modification will have to be controlled on a nanometer scale. To gain full use of FIB techniques a fundamental understanding of the interaction of ion beams with the substrate material is required.

Based on the idea of a catalytic process similar to the VLS approach, Ge, GaSb and Sb nanowires were generated. The nanowires show remarkable uniform diameters in the range of several tens of nanometers and length up to few micrometer. In contrast to a broad class of techniques for nanowires synthesis neither heating of the sample nor any additional materials source is required making this approach compatible to requirements of state of the art on-chip microelectronics.

Furthermore, the realization of extremely high sensitive water and ethanol sensing from individual Sb nanowires is presented. Nanowire sensors are able to convert the presence of a chemical species into electronic information, usually through changes of the nanowire resistivity. For Sb nanowires, electrical characterization during exposure to several gases shows changes in the conductivity up to several orders of magnitude at the appropriate vapor pressure. All the measurements of the impact of the gas on the conduction behavior were operated at room temperature.

## Chapter 2

# Focused Ion Beam System

Ion beams focused to diameters in the range of several tens of nanometers offer an interesting alternative to conventional lithography based pattern techniques. Due to the beam diameter in the nanometer regime, FIB techniques are most suited for fabrication of nanometer sized patterns. It has been found that under certain sputter conditions a periodic height modulation in the form of ripples and dots on a submicron length scale develops during broad beam ion exposure as observed for semiconductor materials [21, 22, 23, 24], metals [25, 26], insulator surfaces [27], and others (e.g., graphite [28]). To gain full use of FIB techniques a fundamental understanding of the interaction of ion beams with the substrate material is required.

### 2.1 FIB Technique

In focused ion beam systems, ions accelerated to energies of several keV are focused to narrow beams with diameters of few nanometers. Such a system basically consists of three parts:

- An ion column consisting of an ion source, an electrostatic lens system, apertures and blanking electrodes needed for ion beam formation.

- A vacuum chamber equipped with a high-precision stage.
- A gas injection system for controlled introduction of gases for deposition and etching.

The system used for the experiments presented in this thesis is shown in Fig. 2.1 and the schematic of the ion column architecture in Fig. 2.2.

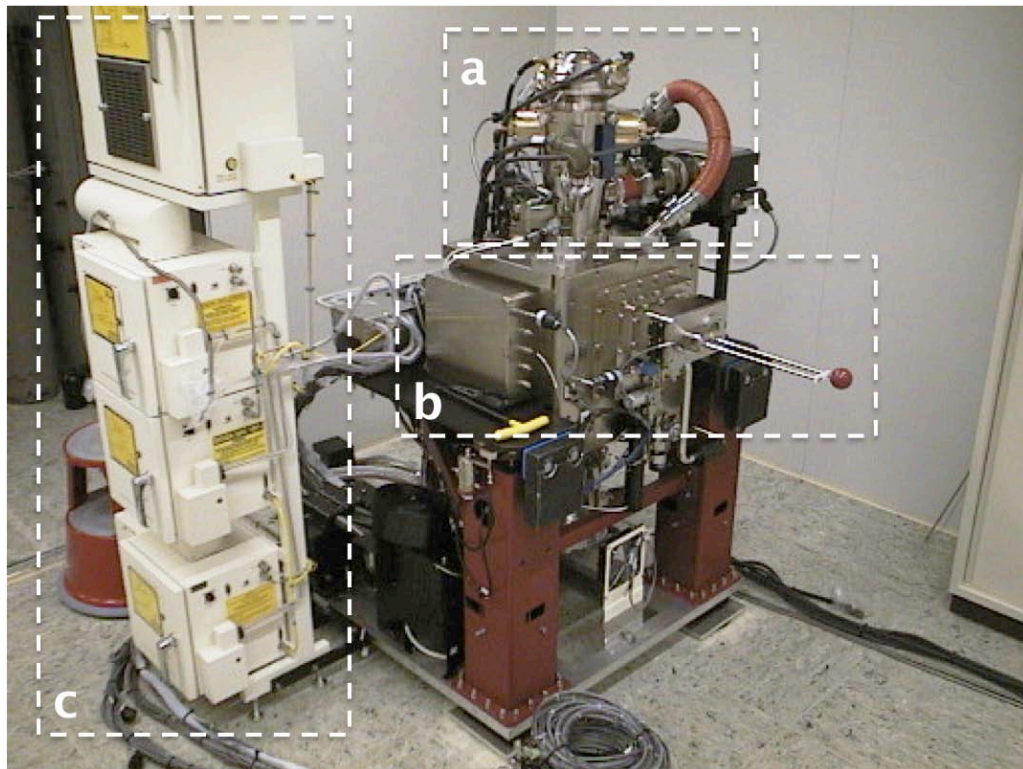


Figure 2.1: Photograph of a Micrion 2500 FIB System. This system can be divided into three main parts: (a) the ion column with the liquid metal ion source on top, (b) the vacuum chamber with the high-precision stage and the load lock, and (c) the gas injection system.

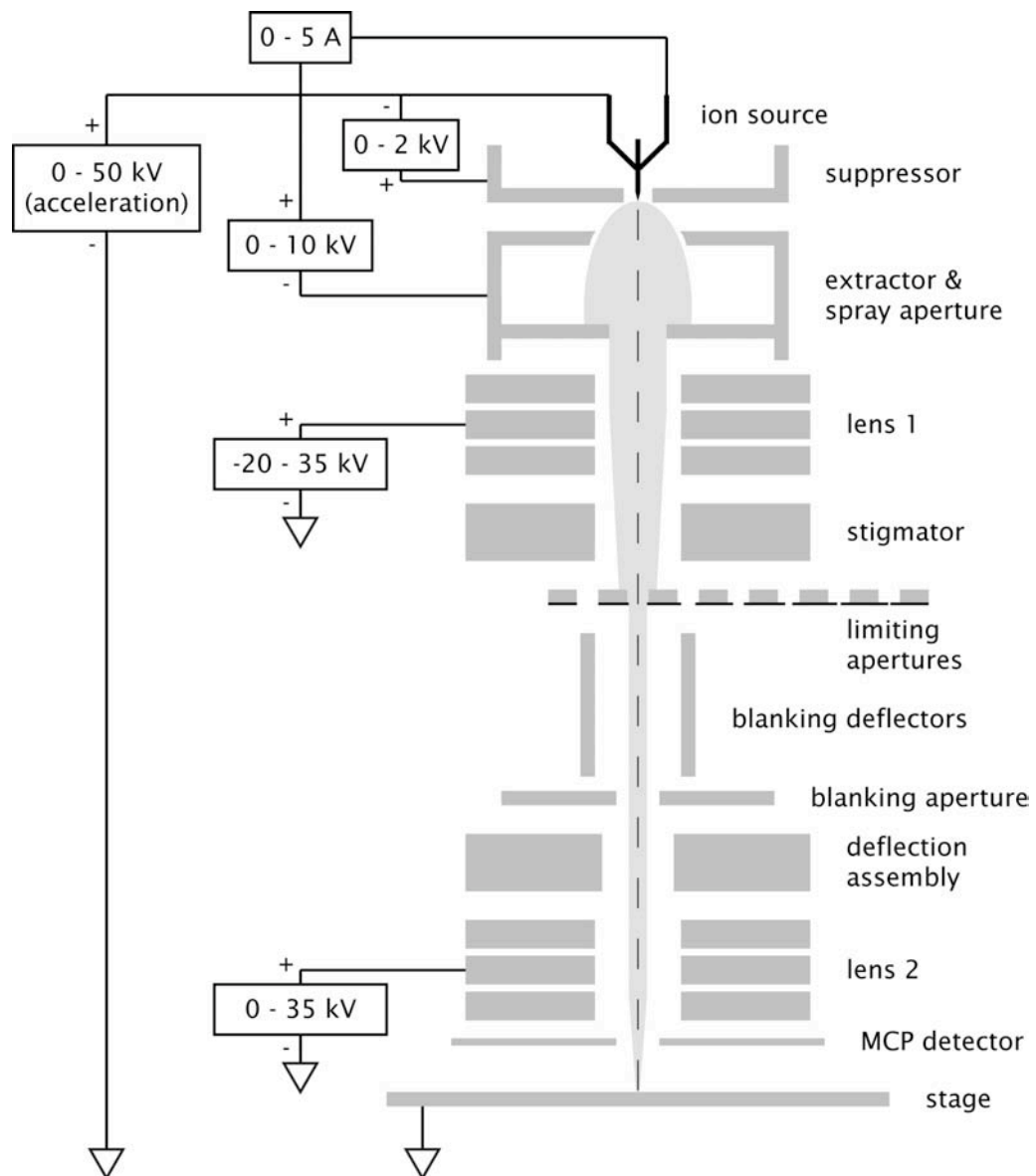


Figure 2.2: Schematic illustration of the ion column architecture of a Micrion 2500 FIB setup.

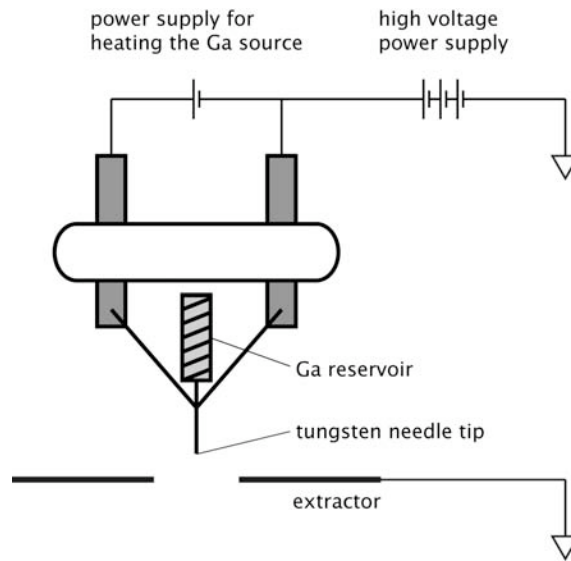


Figure 2.3: Detailed schematic of a liquid metal ion source.

### 2.1.1 Ion Column and Ion Source

The ion column is the core of the whole system. On top of the column the ion source is located. An illustration of a liquid metal ion source equipped with Ga is given in Fig. 2.3. Gallium stands out due to its low melting point at 29,8 °C, the low vapor pressure over a wide range of temperatures and a high surface tension. The ion source consists of a tungsten needle with a sharp tip (radius of approx. 10  $\mu\text{m}$ ) and a reservoir built up by windings of a tungsten wire storing about 2 mm<sup>3</sup> of Ga. In operational mode the tungsten tip is completely covered by a thin Ga film. Opposite of the tip an extractor electrode at negative potential leads to a deformation of the Ga film forming the so-called “Taylor cone”. This results in an actual tip diameter of even below 10 nm [29]. The opposite electrical field provided by the extractor electrode and a field enhancement effect due to this small tip dimensions result in a local field strength of 2 V/Å. This is high enough to extract Ga ions from the cone. The ions leave the source in form of a divergent beam. Most of the ions are collected at the extractor electrode, only a small amount passes the aperture and enters the electrostatic lens system for the formation of a narrow ion beam that finally hits the substrate.



### 2.1.2 Vacuum Chamber

The ion column is stationary and vertically connected to the work chamber, which is the vacuum vessel in which the specimen resides during FIB work. This work chamber is equipped with a high-precision multi-axial stage to position the sample beneath the ion column. Besides motion in the x-y plane and in z-direction, the stage can be tilted allowing a variation of the incidence angle of the ion beam. A load lock system allows the specimen to enter and leave the work chamber without requiring the work chamber to be completely vented and re-pumped. Loading and unloading of samples can be carried out within a few minutes.

### 2.1.3 Gas Injection System

FIB systems can be additionally equipped with gas injection systems needed for gas assisted etching or material deposition. Through individual lines and nozzles different gases can be introduced into the vacuum chamber adsorbing at the sample surface. Gases used for deposition are e.g. W and Pt precursors. As the ions pass through the adsorbed layer, they decelerate rapidly. This results in an energy entry that dissociated the gas molecules and fixes the deposition material on the sample surface. Repetitions of the raster build up successive layers of the material until the desired total layer thickness is reached. This technique can be used e.g. for fabrication of missing electrical contacts in a post-process chip repair.

Besides that highly reactive gases such as  $\text{XeF}_2$  can be used to improve sputter yield. The formation of volatile reaction products reduces redeposition of sputtered material. Thereby the effective etch rate can be multiply enhanced, e.g. by a factor of 7 in case of  $\text{XeF}_2$  and Si substrates [30].

## 2.2 FIB Processing

Exposure of a solid state body to ions with kinetic energies of some keV to some hundred keV leads to deceleration of these ions down to the point of a halt due to their interaction with the atoms of the target material. If the energy transfer is high enough substrate atoms are displaced, in case of a crystalline substrate creating interstitials and voids. If more than 50% of substrate atoms are removed from their origin position the initial crystalline structure is then amorphous. Most FIB processes result in a such a state.

Atoms removed by the incident ions loose their kinetic energy by subsequent impingement with other substrate atoms in form of collision cascades. If such cascades recoil and reach the target surface with an energy above the surface binding energy usually in the range of some eV, a substrate atom is ejected as ion or neutral atom. Besides those secondary atoms and ions, the incident ions also generate secondary electrons. For the purpose of imaging, these electrons are collected with a secondary electron detector. Images as known from secondary electron microscopy generating the secondary electrons by incident electrons can be achieved allowing in-situ imaging while FIB processing. On the path through the solid state body all these collision processes slow down the incident ion. At some point the ion is stopped and remains at its final position as an implanted particle. Fig. 2.4 illustrates the collision cascade of a single incident ion and the generated secondary particles.

The cross section expresses the likeliness of interaction between particles. The more of the kinetic energy per unit length ( $dE/dz$ ) gets lost, the higher is the cross section value. Most FIB processes are carried out at energies between 10 - 50 keV. In this range due to a high cross section the ion energy is basically transferred to surface-near atoms, which results in a high sputter yield of secondary particles. In case of using 50 keV Ga ions and Si substrates a single incident ion generates 10 - 100 secondary electrons and 2 - 3 secondary ions leading to effective material sputtering.

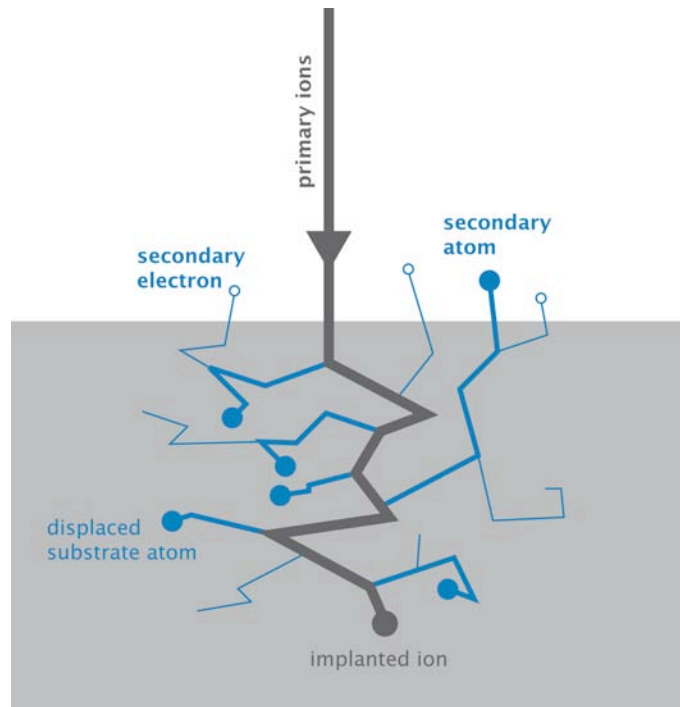


Figure 2.4: Schematic illustration of interaction between high energetic ions and the substrate. The impact of the ions results in displacement of substrate atoms, emission of secondary particles, atoms, ions and electrons, and implantation of ions originating from the ion beam.

## 2.3 Beam Scanning Strategy

For the purpose of structuring the focused ion beam is scanned over a defined area (milling box) in discrete steps with well defined step size (pixel spacing) and dwell time, i.e. the time the beam remains on each single spot. Each scan across the selected area deposits an ion fluence which is correlated to the above mentioned parameters. In the following, single pass milling denotes a scanning strategy where the whole fluence is deposited within one single scan. For multi pass milling, the beam is scanned several times across the predefined area and the number of scan repetitions is determined by the total ion fluence, the step size and the dwell time of the FIB. The guidance of the FIB over the substrate surface is illustrated in Fig. 2.5.

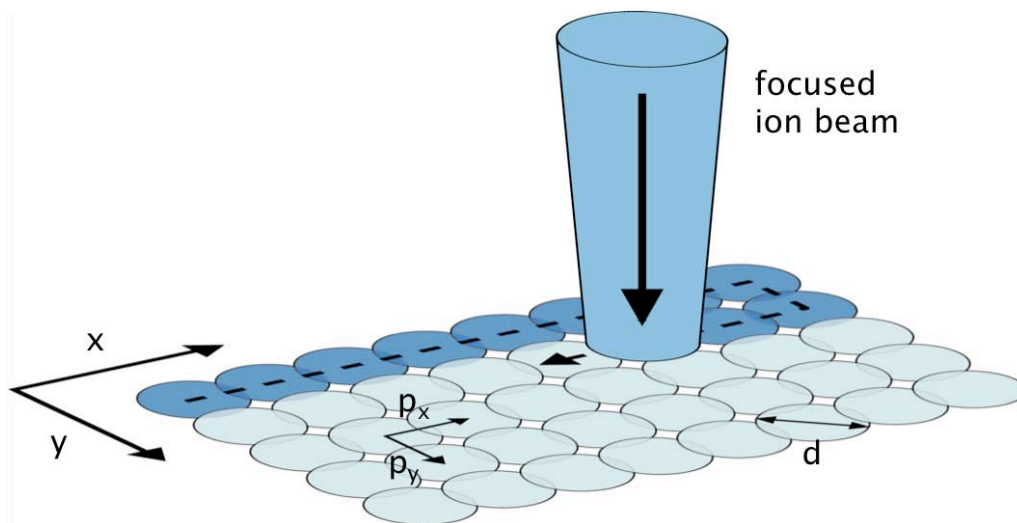


Figure 2.5: Schematic illustration of the FIB scanning strategy. The Ga FIB is sequentially guided in discrete steps over the substrate surface pixel-by-pixel (in x direction) and line-by-line (in y direction) scanning strategy, respectively. The dashed line describes the path of the FIB in single pass mode (in serpentine), " $p_x$ " and " $p_y$ " denote the step sizes, " $d$ " denotes the actual beam diameter irradiating the substrate.

For the purpose of ion beam induced material deposition a further parameter called refresh time, which is the time between two raster scans, is crucial. The adsorption of a new layer of precursor molecules has to be ensured before scanning the next raster. Otherwise already deposited material would be removed by sputtering again. For advanced sputter etching the refresh time leads to full coverage of the surface by reactive gas species thus increasing the sputter yield. In Tab. 2.1 arbitrary parameters and derived parameters resulting from choice of arbitrary ones are listed.

Due to the capability of our system to image during FIB processing, the surface evolution can be observed in-situ by FIB induced secondary electron microscopy (FIB-SEM). This is managed by collecting the generated secondary electrons (SE) in a SE-detector and visualization of electron intensity according to each spot on a display.

arbitrary parameter	symbol	comment
beam current	$I$	depending on aperture
beam diameter	$d$	
ion fluence	$F$	
width of milling box	$w$	x-direction
height of milling box	$h$	y-direction
pixel spacing	$p_x$	x-direction
pixel spacing	$p_y$	y-direction
dwelt time	$t_{dw}$	
refresh time	$t_{ref}$	
derived parameter	symbol	comment
number of pixels	$N_p$	
time for one raster scan	$t_r$	
number of raster scans	$N_r$	
total time	$T$	

Table 2.1: Set of parameters for FIB processing.

## Chapter 3

# FIB Induced Surface Evolution

In this chapter the formation of nanopatterns as a result of the incidence of a focused ion beam onto various substrates is presented. When a sample surface is exposed to the FIB, interaction between accelerated ions and substrate atoms and therefore an evolution of the surface takes place. Carefully adjustment of the FIB parameters such as beam energy, beam diameter and beam current may lead to the formation of a variety of patterns in the nanoscale regime such as nanodots, nanocrystals and nanowires.

### 3.1 FIB Response of GaAs

The exposure of a GaAs sample with a 50 keV focused Ga ion beam leads to decomposition of GaAs [31]. Preferential sputtering of As generates an excess of Ga on the substrate surface. Because of the low melting point of Ga and the surface tension the Ga atoms agglomerate into spherical Ga droplets. The formation of Ga-rich liquid droplets on the surface is shown in the FIB-SEM image in Fig. 3.1(a). Thereby the GaAs surface is exposed to an ion fluence of  $6,2 \times 10^{17}$  ions/cm<sup>2</sup>. In-situ monitoring shows that these dots move around on the surface as long as this area is exposed to the FIB.

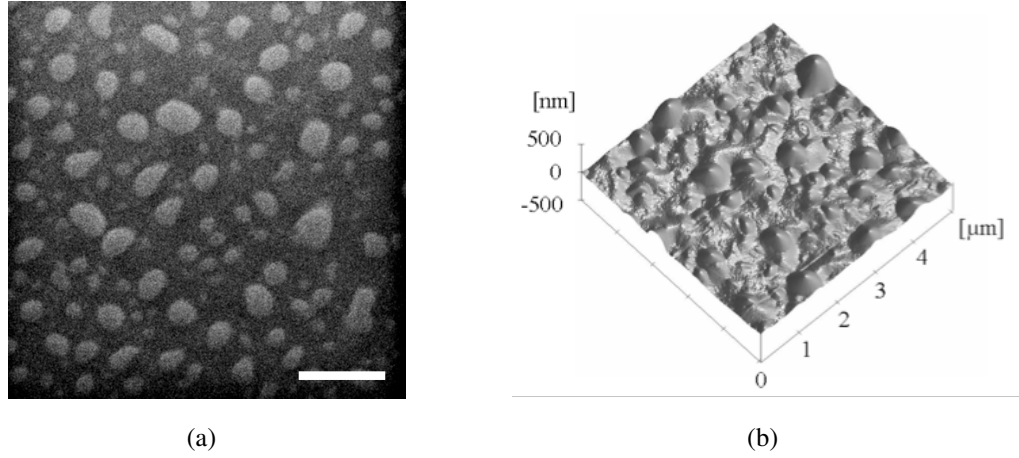


Figure 3.1: The FIB-SEM image in (a) displays the GaAs surface after FIB exposure to 50 keV Ga ions depositing an ion fluence of  $F=6, 2 \times 10^{17}$  ions/cm<sup>2</sup>. Scale bar, 1  $\mu$ m. Topography investigation is done by AFM, the according image is given in (b).

Topography investigations by atomic force microscopy (AFM) visualizes agglomeration of the droplets gathering at lower levels of the roughened surface after FIB milling which is displayed in Fig. 3.1(b).

### Chemical Composition of GaAs dots

The chemical composition of the dots is analyzed by Auger electron spectroscopy (AES). The uppermost reference spectrum in Fig. 3.2 draws the 50:50 stoichiometry of untreated GaAs. The spectrum below (denoted “dot”) gives the measurement performed on a droplet showing that it consists of nearly pure Ga. Finally, it is shown that thermal annealing at 200 °C for 1 min in forming gas leads to elimination of the remaining As content in the droplet (denoted “dot<sub>RTA</sub>”). The resulting AES spectrum shows a high Ga and hardly any As signal.

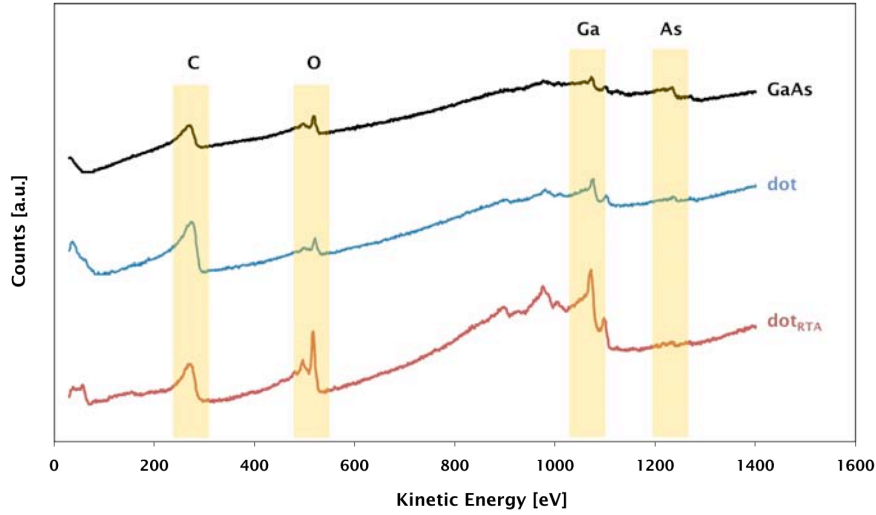


Figure 3.2: AES spectra of untreated GaAs (denoted “GaAs”), a droplet formed during FIB milling (denoted “dot”) and a droplet after a rapid thermal annealing (denoted “dot<sub>RTA</sub>”).

## 3.2 FIB Response of InAs

FIB irradiation of InAs (100) surfaces leads to the formation of randomly distributed protrusions [32, 33]. Sizes ranging from 60 nm to 2  $\mu\text{m}$  and protrusion densities depend on the deposited ion fluence. The SEM image in Fig. 3.3(a) shows raised nanostructures generated at an ion fluence of  $2,5 \times 10^{16}$  ions/cm<sup>2</sup>. Based on AFM investigation as displayed in the topography image in Fig. 3.3(b), these protrusions are suggested to have a crystalline structure as the formation of facets is observed.

### Chemical Composition of In crystallites

The chemical composition of a single crystallite is proved by AES investigation (Fig. 3.4). The upper most line draws the AES spectrum of untreated InAs (denoted “InAs”). The composition of a crystallite formed during FIB milling is given in the spectrum (denoted by “cryst.”) clearly indicating that the crystallite consist of nearly pure In. The ion bombarded region between the protrusions investigated by AES (denoted “IB”) shows a sub-



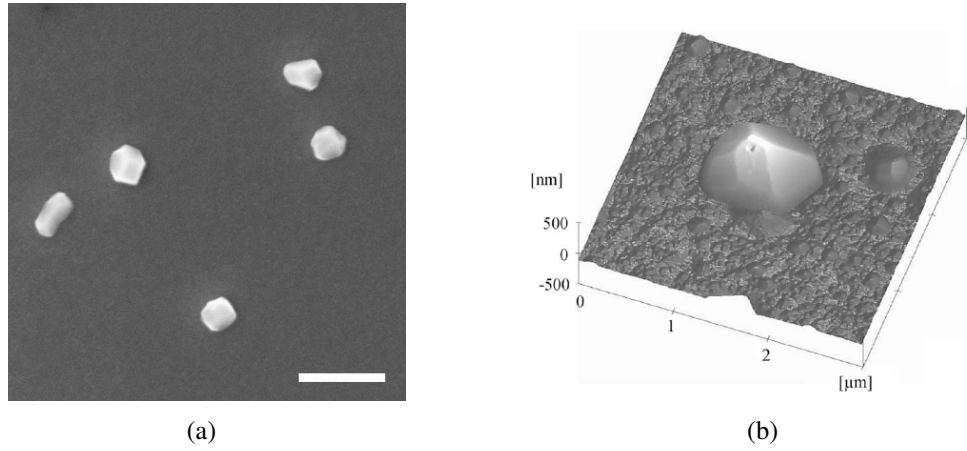


Figure 3.3: The SEM image in (a) shows In crystallites formed on the InAs surface due to FIB exposure with an ion fluence of  $F=2,5 \times 10^{16}$  ions/cm<sup>2</sup>. Scale bar, 1 μm. The AFM image in (b) displays the topography of an even larger crystallite generated by FIB milling with an ion fluence of  $5 \times 10^{17}$  ions/cm<sup>2</sup>.

strate composition very similar to that of an untreated substrate. The formation of In-rich crystallites can again be explained by preferential sputtering and the fact that As is highly volatile.

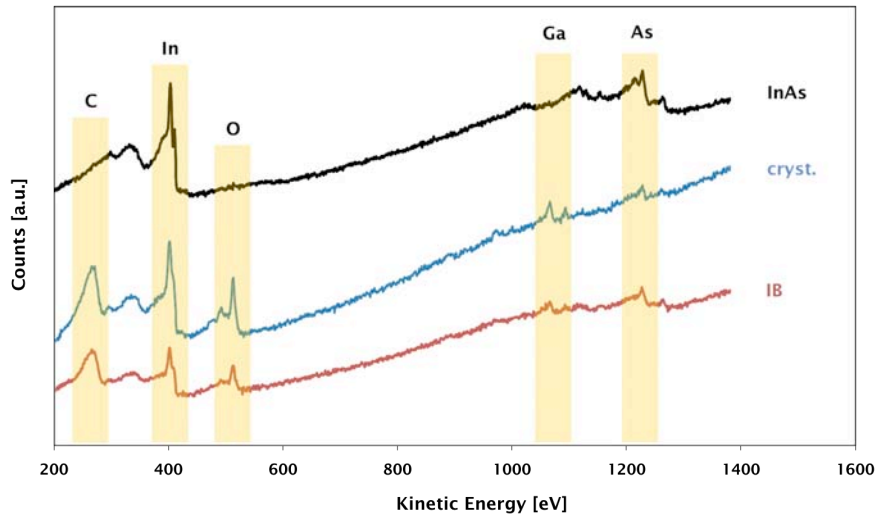


Figure 3.4: AES spectra of untreated InAs (denoted “InAs”), a crystallite formed during FIB milling (denoted “cryst.”) and the ion bombarded region between the crystallites (denoted “IB”).

### Morphological Structure of In crystallites

Finally, X-ray diffraction analysis shown in Fig. 3.5 proves the crystallinity of the resulting nanostructures. After FIB irradiation of the InAs (100) wafer the three most intense reflections of crystalline In are clearly visible and the extracted data is in good agreement with the values given in literature on reference material [34].

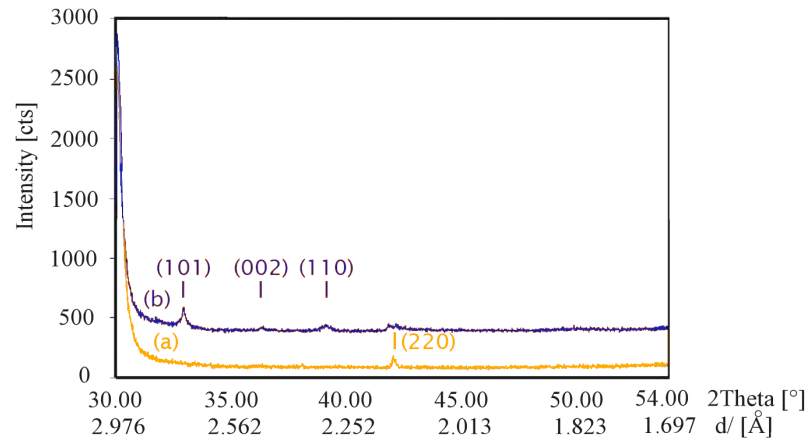


Figure 3.5: X-ray diffractograms of an InAs (100) substrate (a) before and (b) after bombardment by the Ga FIB. Reference reflections of In and InAs are indicated according to literature [34].

## 3.3 FIB Response of Ge

Under certain conditions, Ga FIB exposure of Ge substrates leads to the formation of 1D nanostructures in form of nanowire. Variation of FIB parameters especially such as ion fluence and beam scanning strategy (single pass vs. multi pass mode) is done to find out more about this growth phenomenon.

### Impact of Ion Fluence on Ge

The influence of the ion fluence on the surface evolution of Ge is shown in Fig. 3.6. Fig. 3.6(a) illustrates the Ge sample exposed to an ion fluence of  $6,2 \times 10^{16}$  ions/cm<sup>2</sup> leading to the formation of a nanowire network structure. With an increase of the ion flu-

ence by a factor of 10 as given in Fig. 3.6(b) not only ion exposed sites show an evolution. A different type of nanostructures is generated even beyond the rims of the milling box. Further increasing of the ion fluence results in intense material removal due to sputtering on the one hand and generation of nanowires with lengths of some microns outside this area on the other hand.

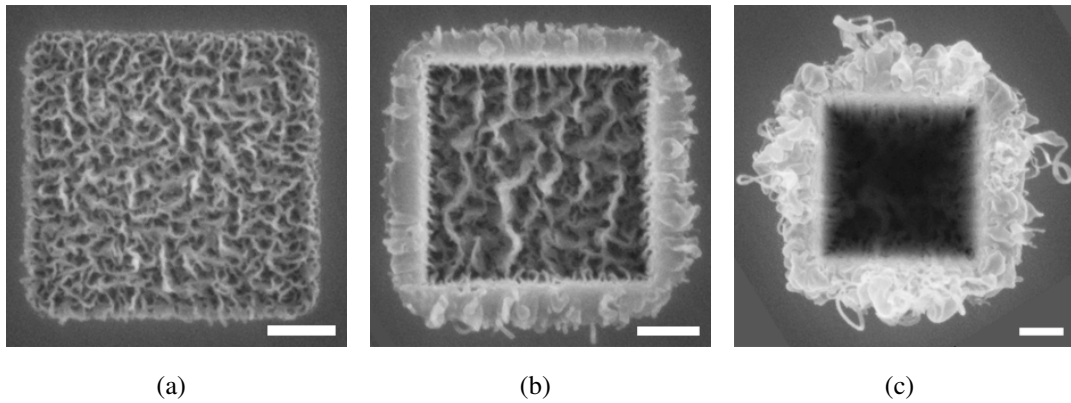


Figure 3.6: Ga FIB resonance of Ge. The substrates are exposed to an ion fluence of (a)  $F=6,2 \times 10^{16}$  ions/cm<sup>2</sup>, (b)  $F=6,2 \times 10^{17}$  ions/cm<sup>2</sup>, and (c)  $F=6,2 \times 10^{18}$  ions/cm<sup>2</sup>. Scale bars, 500 nm.

### Impact of Scanning Strategy on Ge

The scanning strategy has a major impact on the appearance of the FIB irradiated regions and the surrounding area. The SEM images in Fig. 3.7 show both milling boxes exposed to an ion fluence of  $6,2 \times 10^{18}$  ions/cm<sup>2</sup>. In Fig. 3.7(a) the beam was guided 2500 times across the milling box until the whole ion fluence is deposited. This results in a deep sputtered hole which is surrounded by nanowires. With the single pass scanning strategy shown in Fig. 3.7(b) the beam is moved over the sample surface only once. The last scanning line is noticeable. The before scanned lines are partly refilled by redeposited material, partly overgrown by nanowire structures. As no following raster scan is performed they are not destroyed by further FIB milling.

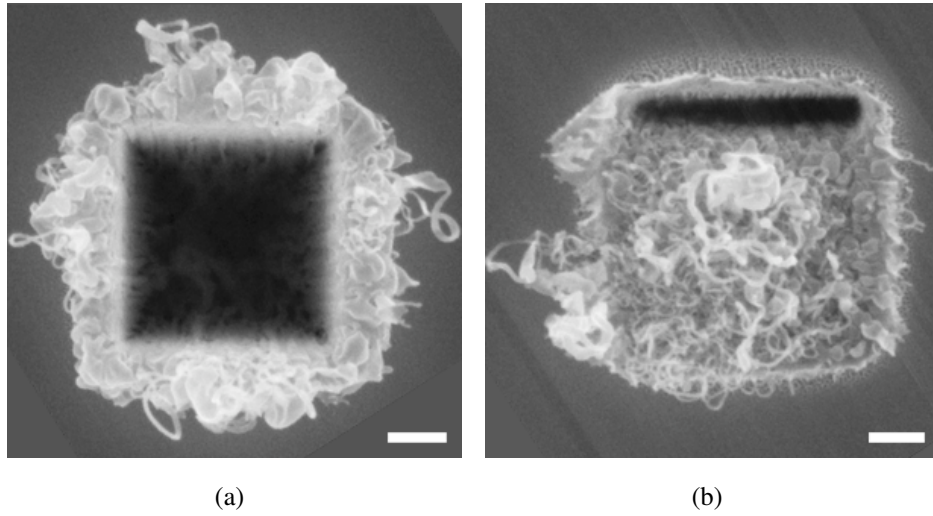


Figure 3.7: Comparison of the impact of the scanning strategy for Ge. In (a) the FIB is guided over the Ge sample surface with a dwell time of  $5 \mu\text{s}$  in 2500 rasters until the whole predefined ion fluence is deposited, in (b) the beam is moved over the surface only once depositing the same ion fluence of  $F=6,2 \times 10^{18} \text{ ions/cm}^2$ . Scale bars, 500 nm.

### 3.4 FIB Response of GaSb

The impact of the FIB on GaSb surfaces with increasing ion fluence can easily be retraced by the SEM images in Fig. 3.8. At the very beginning of the FIB exposure process many honeycomb-like cells are generated in a subsurface region. The incidence of ion beam creates a lot of vacancies and interstitials by displacing substrate atoms from their initial sites. Vacancies accumulate and over-saturate in the irradiated region forming voids. [35]. Ongoing milling leads to a transformation of the comb structure into a sponge-like network and some precipitations atop.

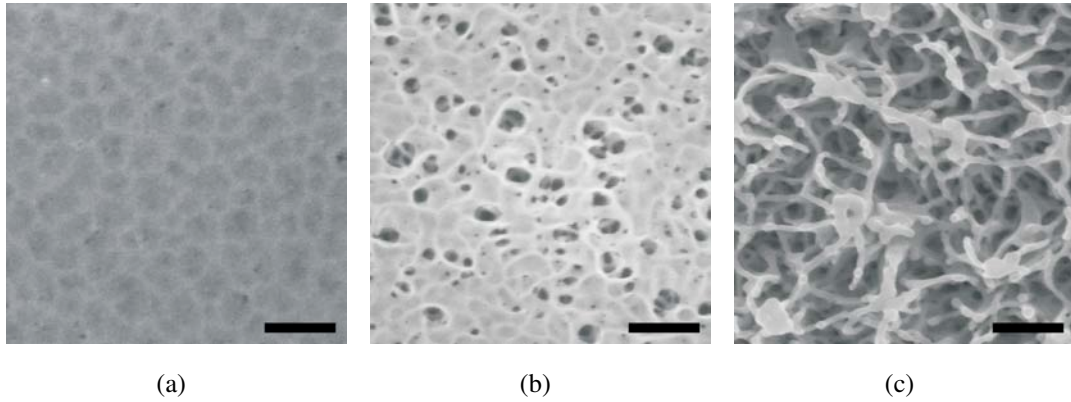


Figure 3.8: SEM images of GaSb surface evolution depending on the ion fluence. In (a), an ion fluence of  $F=3,1 \times 10^{13}$  ions/cm<sup>2</sup> leads to a subsurface formation of honeycomb-like structures, in (b) the surface becomes more and more porous (ion fluence of  $F=6,2 \times 10^{13}$  ions/cm<sup>2</sup>) until a transformation into a sponge-like network as shown in (c) takes place with an ion fluence of  $F=3,1 \times 10^{14}$  ions/cm<sup>2</sup>. Scale bars, 200 nm.

### Chemical Composition and Morphological Structure of GaSb Sponge

AES measurements in Fig. 3.9 show that the nanowires building up this sponge consist of Ga and Sb in the same ratio as the untreated GaSb substrate. The according AES spectra are denoted “GaSb” for untreated GaSb and “sponge” for the nanowire network structure. The droplet-like structures observed on top of these wires are determined to be Ga. The nanowires precipitate even at places just beyond the rim of the milling box, which are not directly exposed to the FIB. The diameters measure in the range of several tens of nanometers. High resolution transmission electron microscopy (HRTEM) image in Fig. 3.10 of such wires shows the crystal texture of a single nanofiber. Expanded crystalline regions can be observed.

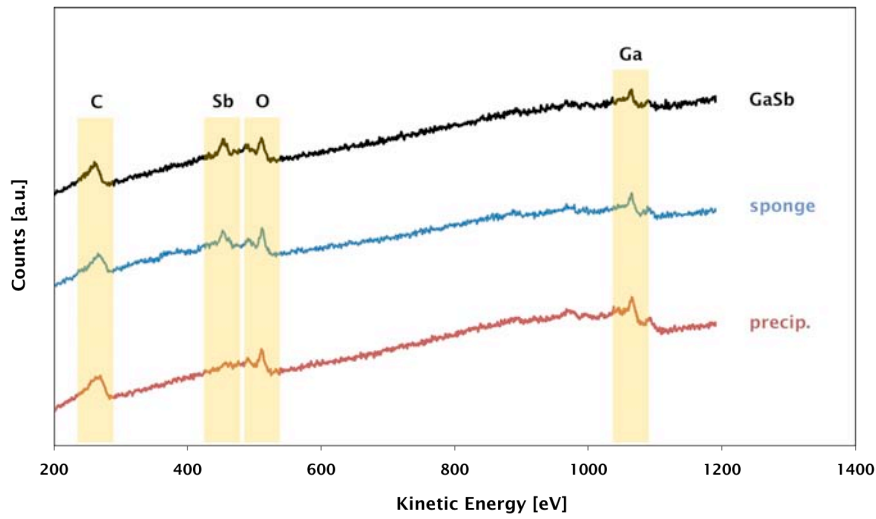


Figure 3.9: AES spectra of untreated GaSb (denoted “GaSb”), fibers building up the sponge-like structure (denoted “sponge”) and a Ga rich precipitations on top of these nanowires (denoted “precip.”).

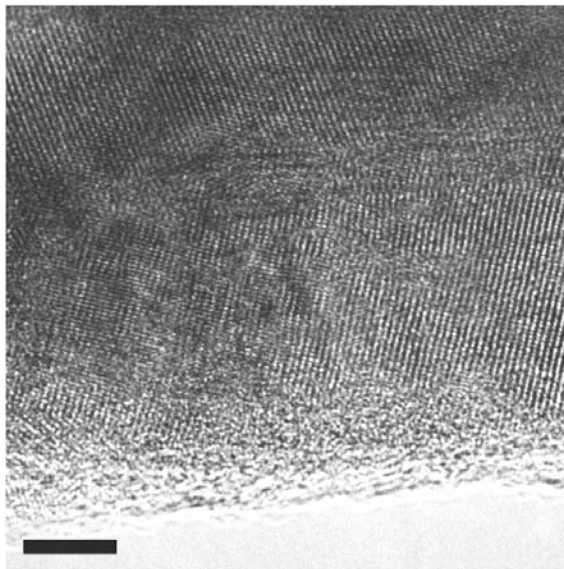


Figure 3.10: HRTEM image of a single GaSb nanowire with crystalline regions. Scale bar, 5 nm.

### Impact of Ion Fluence on GaSb

The SEM images of GaSb surfaces exposed to ion fluences of  $6,2 \times 10^{16}$  ions/cm<sup>2</sup> and  $6,2 \times 10^{17}$  ions/cm<sup>2</sup> in Fig. 3.11 show the impact of this parameter on the FIB exposed substrate. In contrast to Ge substrates, a rather dense nanowire network is generated at comparable low ion fluences inside the milling boxes as displayed in Fig. 3.11(a). The clearly visible formation of a nanowire network outside the irradiated zones is remarkable as these areas have never been treated by the Ga FIB.

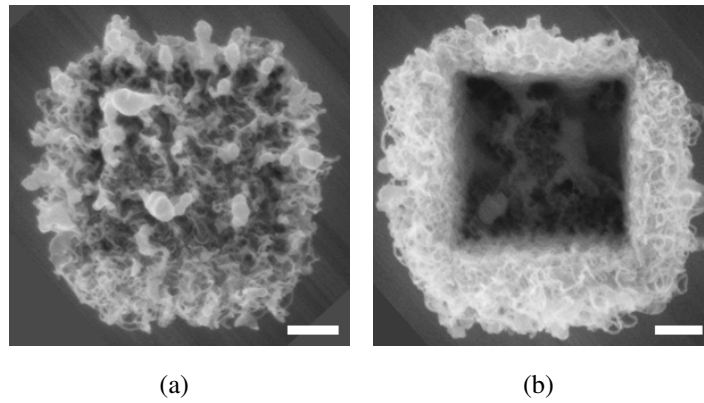


Figure 3.11: SEM images of GaSb exposed to the FIB with an ion fluence of (a)  $F=6,2 \times 10^{16}$  ions/cm<sup>2</sup> and (b)  $F=6,2 \times 10^{17}$  ions/cm<sup>2</sup>. Scale bar, 500 nm.

### Impact of Scanning Strategy on GaSb

The impact of the scanning strategy (multi pass vs. single pass) is shown in Fig. 3.12. Although depositing the same total ion fluence the resulting patterns look completely different. Fig. 3.12(a) shows that FIB milling of the box results in a deep sputtered hole. A dense nanowire network is observed beyond the rims, where growth without being bothered by FIB irradiation takes place. The single pass processed surface shown in Fig. 3.12(b) looks very grainy without a comparable deep sputtered box.



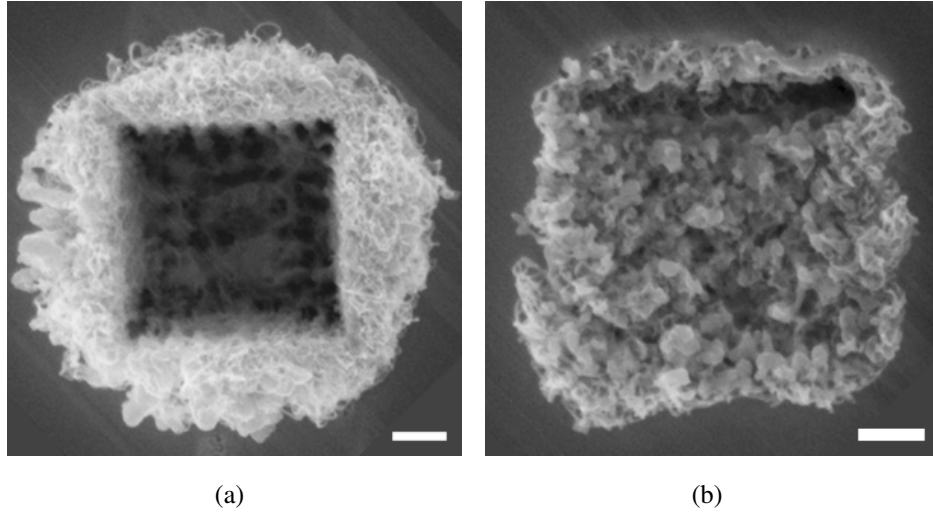


Figure 3.12: Impact of the scanning strategy on nanowire growth. For the purpose to depositing a total ion fluence of  $F=6,2 \times 10^{17}$  ions/cm<sup>2</sup>, (a) represents multi pass milling of the FIB rastering over the GaSb sample surface with a dwell time of 5  $\mu$ s in 250 rasters, (b) shows the result of single pass processing. Thereby the whole predefined ion fluence is deposited in one single raster scan. Scale bar, 500 nm.

### 3.5 FIB Response of Sb

FIB milling of Sb substrates leads to generation of nanowires, several  $\mu$ m long and very uniform in diameter in the range of 25 nm.

#### Impact of Ion Fluence on Sb

In Fig. 3.13 SEM images of Sb substrates after FIB milling with various ion fluences are displayed. Fig. 3.13(a) shows the Sb sample exposed to an ion fluence of  $6,2 \times 10^{16}$  ions/cm<sup>2</sup>. Nanostructures in form of loose wires more concentrated at the upper rim of the box are observed. An increase of the ion fluence to  $6,2 \times 10^{18}$  ions/cm<sup>2</sup> shown in Fig. 3.13(c) results in development of dense nanowire network outside the irradiated zones is very intense. The resulting network structures reach several  $\mu$ m beyond the rims.



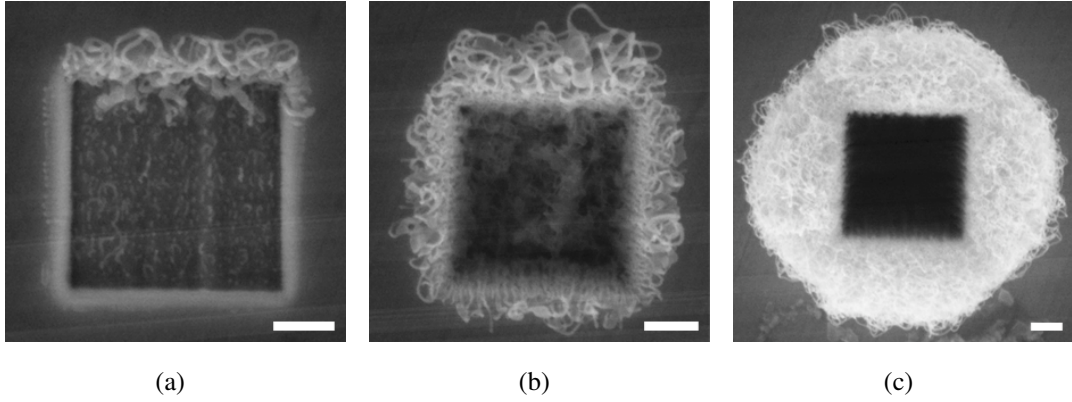


Figure 3.13: SEM images of Sb surfaces FIB exposed to ion fluences of (a)  $F=6,2 \times 10^{16}$  ions/cm<sup>2</sup>, (b)  $F=6,2 \times 10^{17}$  ions/cm<sup>2</sup>, and (c)  $F=6,2 \times 10^{18}$  ions/cm<sup>2</sup> all processed in multi pass scanning mode. Scale bar, 500 nm.

### Impact of Scanning Strategy on Sb

Fig. 3.14(a) shows a SEM image of the Sb surface after multi pass milling of a  $(2 \times 2) \mu\text{m}^2$  wide box with an ion fluence of  $6,2 \times 10^{18}$  ions/cm<sup>2</sup>. As expected, FIB exposure leads to effective sputtering of the substrate material. The rim of the several micrometer deep hole is surrounded by a dense network of nanowires. Milling the same box (with the same total ion fluence) in single pass mode leads to the formation of a pattern shown in Fig. 3.14(b). The FIB scan starts in the upper left of the box and moves along in serpentine. The whole FIB modified area is covered by nanowires with the exception of the last line scan, where the FIB is routed from the lower right to the lower left edge. Nanowires reach even  $2 \mu\text{m}$  beyond the rim of the FIB milled area.

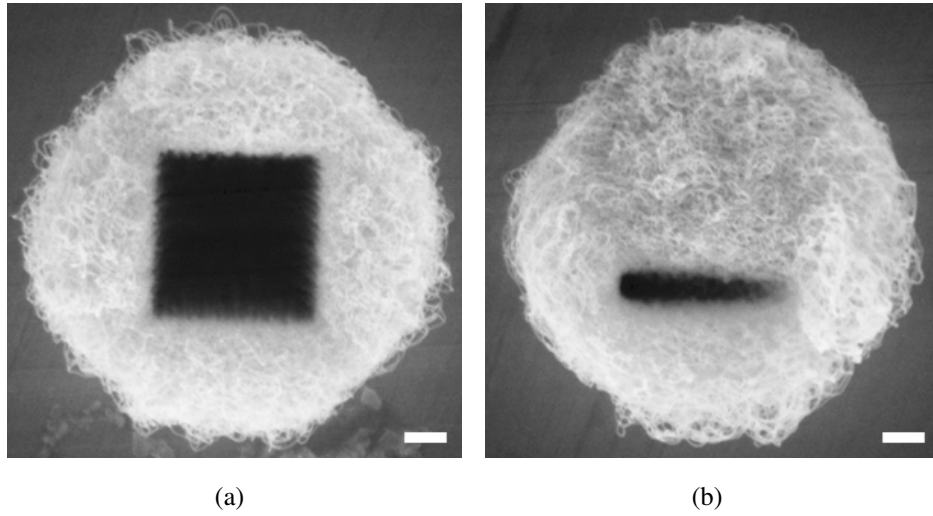


Figure 3.14: SEM image of Sb exposed to the FIB depositing the an ion fluence of  $F=6,2 \times 10^{18}$  ions/cm<sup>2</sup>. In (a) the FIB is guided over the Sb sample surface with a dwell time of  $5 \mu\text{s}$  on and on until the whole predefined ion fluence is transferred, in (b) the beam is moved over the surface only once. Scale bar, 500 nm.

### Position Controlled Growth of Sb Nanowires

Intentional positioning of nanowires is an important requirement for future device integration. Prepatterning of the substrate enables site controlled growth of the nanowires.

As shown in the SEM image in Fig. 3.15(a) an array of FIB sputtered shallow holes is processed. After an additional nearby uniform FIB exposure single nanowires grow out of the pre-processed holes. Fig. 3.15(b) displays the FIB exposed surface after depositing an even higher fluence. Distinctive bundles of nanowires stick out of each single hole. In addition to that formation of wirelike structures in between the holes is observed.

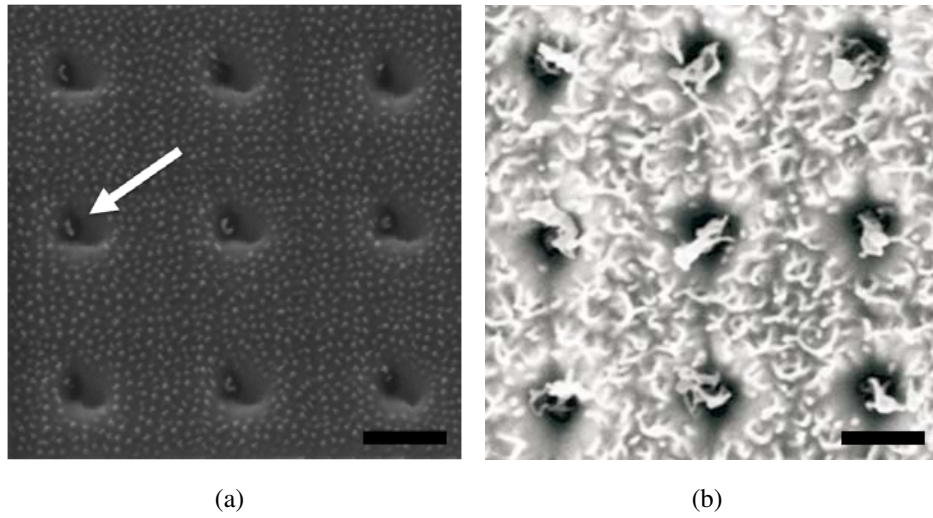


Figure 3.15: SEM images of prepatterned Sb surfaces. In (a), FIB milling of an array of shallow holes leads to preferential growth of single nanowires at these sites (indicated by arrow). Ongoing FIB milling as shown in (b) results in bundles of the nanowires and wire-like structures all over the exposed area. Scale bar, 500 nm.

## Chapter 4

### FIB induced Growth of Sb Nanowires

If Sb substrates are exposed to high energy Ga ion beams, aside of the expected material removal by physical sputtering, the formation of small dots- and wire-like structures is observed. This offers a new approach for the sythesis of Sb nanowires. The SEM image in Fig. 4.1 shows a Sb surfaces exposed to an ion fluence of  $6,2 \times 10^{16}$  ions/cm<sup>2</sup> using a 50 keV Ga FIB. FIB milling of Sb even at comparable low ion fluences leads to precipitation of nanostructures. Bright dots with diameters in the range of 20 nm to 30 nm and an average density of approximately 200 dots/ $\mu\text{m}^2$  are generated. These dots can be interpreted as seeds for nanowire growth. The diameters of the roughly 300 nm long nanowires appear very uniform and are in the range of about 25 nm.

Fig. 4.2(a) shows a SEM image of the Sb surface after multi pass milling of a  $(2 \times 2) \mu\text{m}^2$  wide box with an ion fluence of  $6,2 \times 10^{18}$  ions/cm<sup>2</sup>. As expected, FIB exposure leads to effective sputtering of the substrate material with a high sputter yield  $Y$  of 14,3 Sb atoms per incident Ga ion approximately. The several micrometer deep hole is surrounded by a dense network of nanowires, which show very uniform diameters in the range of 25 nm. Milling the same box in single pass mode leads to the formation of a pattern shown in Fig. 4.2(b). Thereby the FIB scan starts in the upper left corner of the box and moves along in serpentines. Pixel and line spacing are both 10 nm, which for the given FIB diameter guarantees a nearly uniform ion fluence distribution (>99%) [36]. The whole FIB modified area is covered by nanowires with the exception of the last

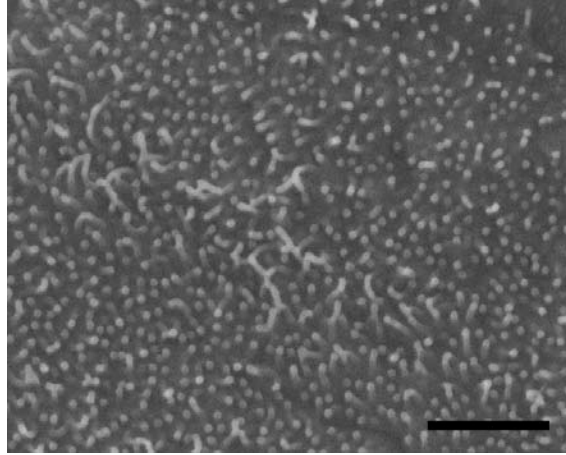


Figure 4.1: SEM image of the Sb surface after FIB exposure with an ion fluence of  $F=6,2 \times 10^{16}$  ions/cm<sup>2</sup>. FIB milling of Sb even at comparable low ion fluences leads to precipitation of nanostructures. The bright dots seem to act as seeds for nanowire growth, some of them have already started growing. The nanowire diameters are very uniform and of about 25 nm in diameter. Scale bar, 500 nm.

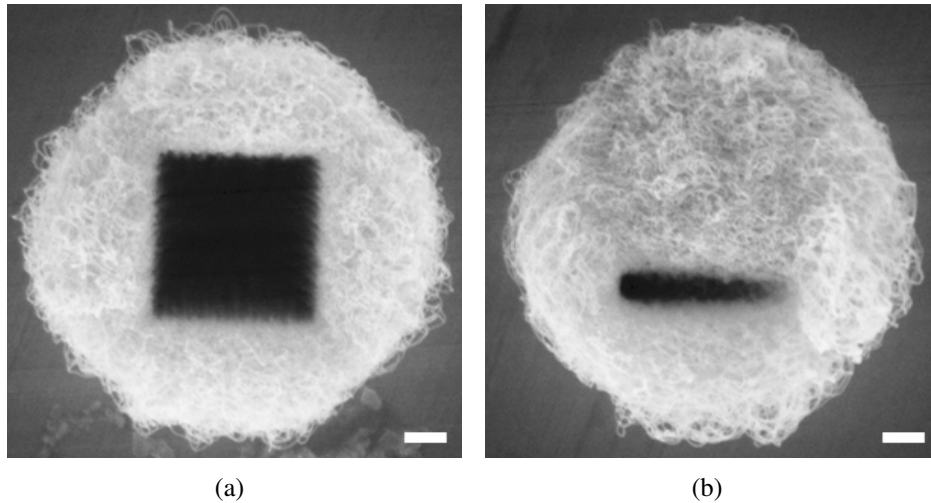


Figure 4.2: SEM image of a FIB processed Sb surface irradiated by an ion fluence of  $F=6,2 \times 10^{18}$  ions/cm<sup>2</sup> in (a) multi pass mode and (b) single pass mode. At these ion fluence the milling box is typically surrounded by a dense network of nanowires reaching up to 2  $\mu$ m beyond the rim of the FIB milled area. Scale bars, 500 nm.

line scan routed from the lower right to the lower left edge. Nanowires reach even  $2\ \mu\text{m}$  beyond the rim of the FIB milled area.

## 4.1 Vertical Uplifting of a Nanowire Network on Sb

With single pass mode the FIB generated nanowire network does not form a plane porous disc as one could assume from the top view SEM image in Fig. 4.2(b). As illustrated in the SEM image in Fig. 4.3(a) and in the schematic illustration in Fig. 4.3(b), the nanowires appear on a ramp-like base normal to the plane rising along the scan direction of the FIB.

The formation of this ramp-like structure is a result of the pixel-by-pixel and accordingly of the line-by-line scanning strategy. Scanning the first line of the predefined milling area leads to nanowire growth even beyond the ion irradiated region. By the guidance of the FIB through the subsequent lines in serpentine, nanowires which were grown on the not yet exposed part in the forefront of the scanning beam are removed by sputtering. Nanowires in already irradiated zones, i.e. behind the scanning beam, remain unaffected.

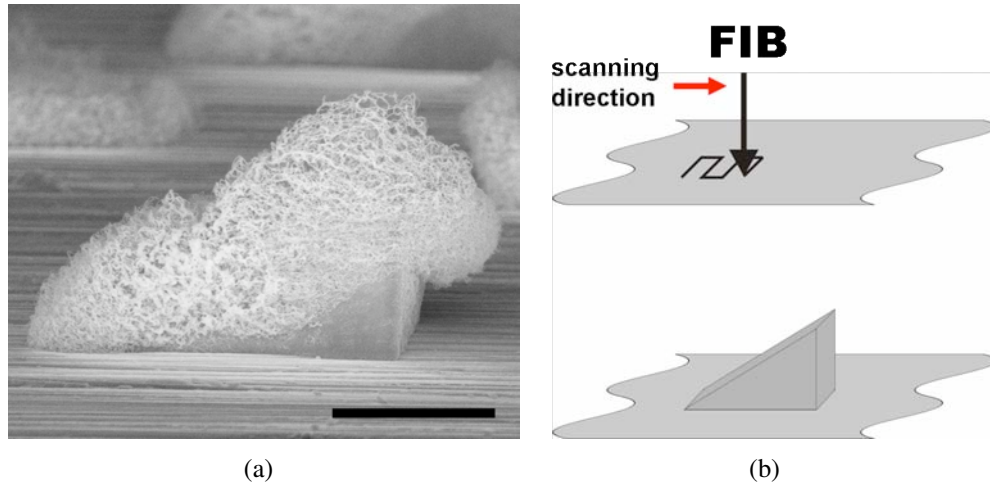


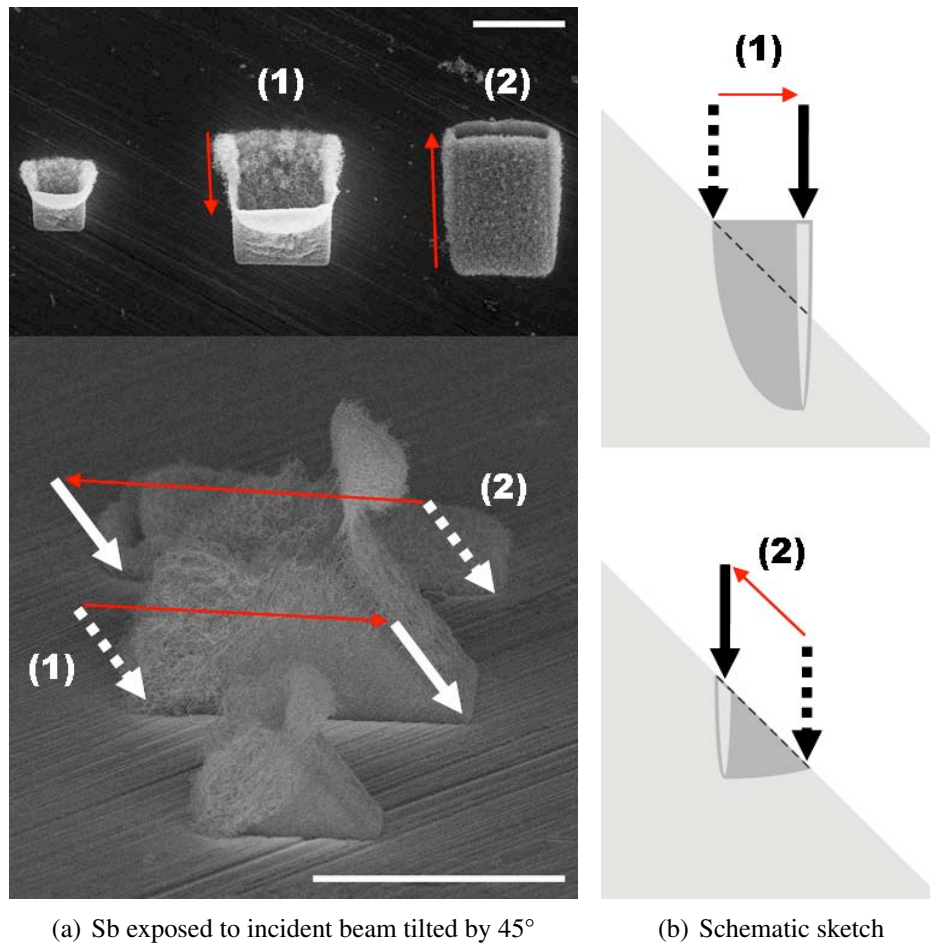
Figure 4.3: In the SEM image in (a) a single pass processed  $(10 \times 10)\ \mu\text{m}^2$  box (ion fluence of  $F = 3.1 \times 10^{18}$  ions/ $\text{cm}^2$ ) is viewed under a tilt angle of  $75^\circ$ , bar scales  $5\ \mu\text{m}$ , (b) gives a schematic sketch visualizing the FIB scanning strategy and the resulting uplifted nanowire network in single pass scanning mode, the black arrow indicates the incident ion beam, the serpentine-like structure gives the current scanning direction and therefore the path of the beam.

These nanowires form a network which is further densified by redeposited Sb. Due to the ongoing FIB scanning this nanowire network reduces the escape angle for the sputtered Sb and more and more of them are picked up by the network which leads to an upraising of the structures.

Accordingly, FIB milling under oblique angles as schematically shown in Fig. 4.4 should lead to an increase or decrease of the uplifting effect due to the variation of the escape angles for sputtered Sb. The results obtained for FIB processing of a Sb surface tilted by  $45^\circ$  relative to the incident focused ion beam are shown in Fig. 4.4(a). Depending on the scanning direction of the FIB the escape angles of the sputtered substrate material change. The scanning direction from higher to lower levels denoted as track (1) in the schematic of Fig. 4.4(b) (escape angle of  $135^\circ$ ) results in an upraised structure. Hardly any uplifting can be observed when scanning in the opposite direction denoted as track (2) (escape angle  $45^\circ$ ). The smaller  $(5 \times 5) \mu\text{m}^2$  FIB milled box in Fig. 4.4(a) (the left box in the top view and the one in front of the side view image) shows the impact of the box length on this uplifting effect. The height of the uplifting increases with the length of the FIB milled box.

A set of exposures under different sample surface to incident beam angles is shown in Fig. 4.5. Investigation of this parameter should give some information of the impact on the resulting uplifted structure. Based on the observation presented before systematic experiments are carried out including all possible scan directions and tilting angles of incident beam towards the sample surface. The top edges of the images are always aligned to upraised surface levels due to tilting, the bottom lines accordingly correspond to lowered surface levels. The arrows indicate the scanning direction of the FIB. All exposed boxes measure  $(5 \times 5) \mu\text{m}^2$  and are processed in single pass mode as no uplifting is observed with multi pass milling. The ion fluence deposited is  $3,1 \times 10^{18}$  ions/cm<sup>2</sup>. Beginning with normal incidence of the ion beam on the substrate in Fig. 4.5(a) all 4 SEM images of course look identically. Tilting the stage the sample is mounted on in  $30^\circ$  steps enables exposure under incidence angles of  $30^\circ$  (Fig. 4.5(b)) and  $60^\circ$  (Fig. 4.5(c)). The evolution of the generated patterns can be easily observed, as the structures among each other are all processed in the same scanning direction. As single pass scanning is always carried out in serpentines, the sideways scanning boxes combine both, the reduced and the ex-



(a) Sb exposed to incident beam tilted by  $45^\circ$ 

(b) Schematic sketch

Figure 4.4: SEM images of areas milled under an angle of incidence of  $45^\circ$ . In the upper part a top view image is given, beneath a side view shows the resulting structures performed under different scanning directions according to the tilted sample surface. Track (1) denotes a FIB guidance from higher to lower surface level, track (2) denotes the opposite direction. The white arrows mark the incident direction of the FIB (the dotted arrows denote the start position, the drawn through arrows the end position of the beam path), the red arrows show the scanning direction. Scale bars,  $10\ \mu\text{m}$ . In (b), a principle sketch to point out the guidance of the FIB and the resulting structure formation is shown.



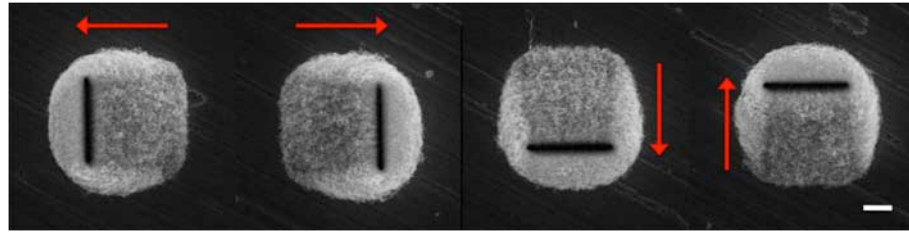
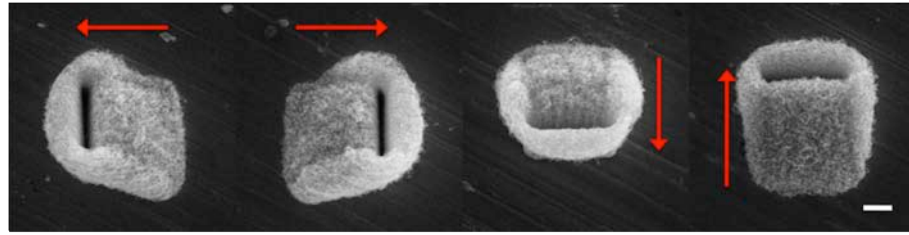
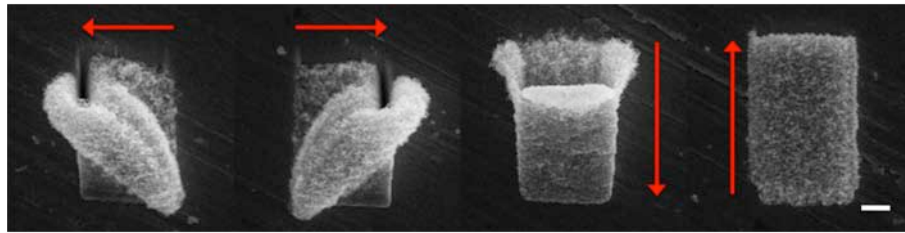
(a) Ion beam incidence angle of  $0^\circ$  (normal incidence)(b) Ion beam incidence angle of  $30^\circ$ (c) Ion beam incidence angle of  $60^\circ$ 

Figure 4.5: Plane view SEM images of variation of incident beam angles exposing the Sb substrate. In (a) ion beam exposing of the Sb substrate under an incidence angle of  $0^\circ$  (normal incidence) is shown, (b) shows the same boxes milled with in incidence angle of  $30^\circ$ , in (c) FIB exposure is performed at the maximum tilting angle resulting in an ion incidence angle of  $60^\circ$ . The top edges of the images always indicate the upraised surface levels. Scale bars,  $2\ \mu\text{m}$

panded escape angle within one milling box depending on the current scanning direction of according line. This results in uplifting structures shown in the two milling boxes on the left in each image row of Fig. 4.5.

Ramp-like structure formation at various scanning lengths is shown in the SEM image in Fig. 4.6. Single pass processed structures each with a width of  $5\ \mu\text{m}$  and lengths varying from 5 to  $50\ \mu\text{m}$  impressively display the uplifting effect. All resulting patterns show ramp-like shapes, which heights saturate at about  $5\ \mu\text{m}$  after  $10\ \mu\text{m}$  FIB scanning. It is remarkable that the sidewalls where the beam shifts its direction grow to a higher level

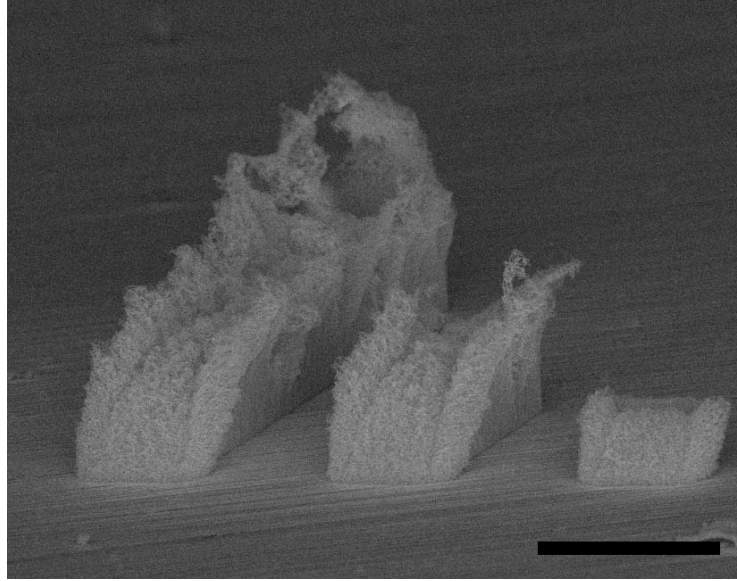


Figure 4.6: Single pass FIB milling of boxes of 5  $\mu\text{m}$  in width and varying scanning lengths of 5  $\mu\text{m}$ , 20  $\mu\text{m}$  and 50  $\mu\text{m}$  (from right to left) each processed with an ion fluence of  $F=3,1\times 10^{18}$  ions/ $\text{cm}^2$ . The SEM image displays the resulting structures under a tilted angle of  $75^\circ$  off-axis. The scale bar denotes 10  $\mu\text{m}$ .

than the area in between. This may be again explained by the reduced escape angle for the sputtered substrate material.

## 4.2 Depth Profile of a FIB Milled Box on Sb

Cleaving a Sb substrate with several  $(10\times 10)\mu\text{m}^2$  milled boxes (Fig. 4.7(a)) gives insight of the depth profile of the nanowire network. The cross sectional view of such a milling box in the SEM image in Fig. 4.7(b) shows the porous re-grown material atop but also the depth profile underneath the sample surface. Here, the range of the porous nanowires network generated by the impact of the FIB with an ion fluence of  $3,1\times 10^{18}$  ions/ $\text{cm}^2$  reaches about 3  $\mu\text{m}$  in depth.

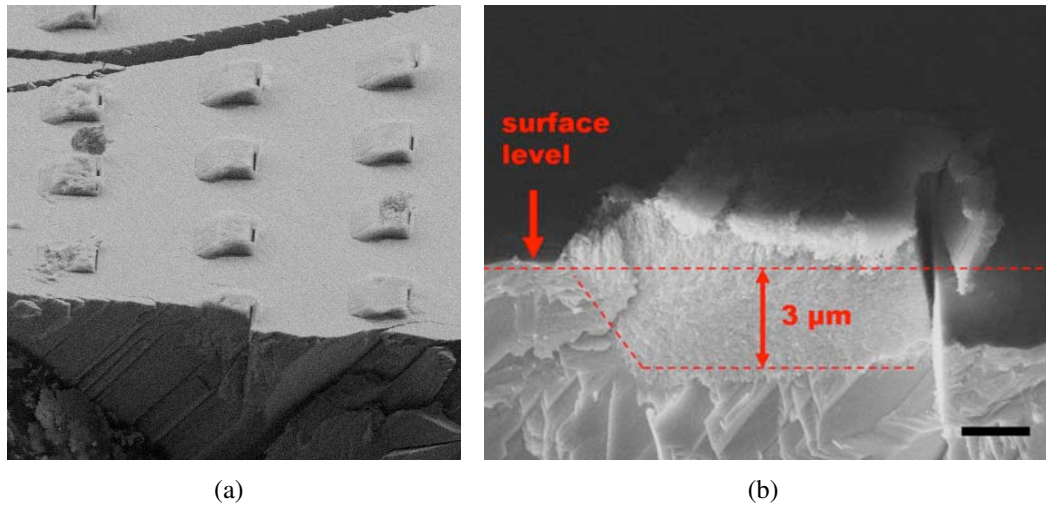


Figure 4.7: Cross section view of the cleaved Sb sample. Before cleaving an array of  $(10 \times 10) \mu\text{m}^2$  boxes has been FIB processed. In (a) the cleaving edge exactly passing one of the FIB processed boxes is shown. In (b) the range of the amorphous network-like structure generated by the impact of the FIB with an ion fluence of  $F=3,1 \times 10^{18}$  ions/cm<sup>2</sup> reaching about 3  $\mu\text{m}$  beneath the substrate surface level is shown.

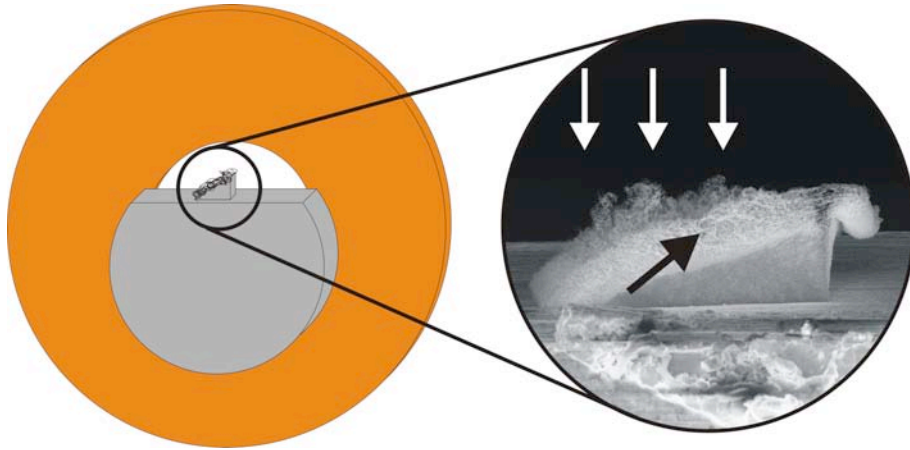


Figure 4.8: Sb sample preparation for TEM investigation. A Sb lamella less than 100  $\mu\text{m}$  thick is mounted on a copper ring for handling with the TEM specimen holder. After that the Sb sample is exposed to the FIB to generate uplifted structures for TEM analysis.

### 4.3 TEM Analysis of Individual Sb Nanowires

To gain information about the crystallographic texture, individual Sb nanowires are analyzed by means of transmission electron microscopy (TEM). For that purpose a thin slice of Sb is mounted on a TEM holder prior to the FIB milling. In the next step FIB processing in single pass mode generates the desired uplifted nanowire network on a cleaved edge as shown in Fig. 4.8. The white arrows denote the incidence direction of the ion beam raster scanned over the Sb substrate surface, the black arrow indicates the incident electron beam for TEM analysis. This special setup enables high resolution transmission electron microscopy (HRTEM), energy dispersive X-ray analysis (EDX) and selected area electron diffraction (SAED) of individual nanowires without any further sample preparation.

TEM investigation proves that the diameter of the Sb nanowires of about 25 nm is widely independent of the processing parameters as shown in the inverted dark field TEM image in Fig. 4.9. The HRTEM image and the inserted SAED pattern in Fig. 4.10 show the amorphous structure of the as-grown Sb nanowire.

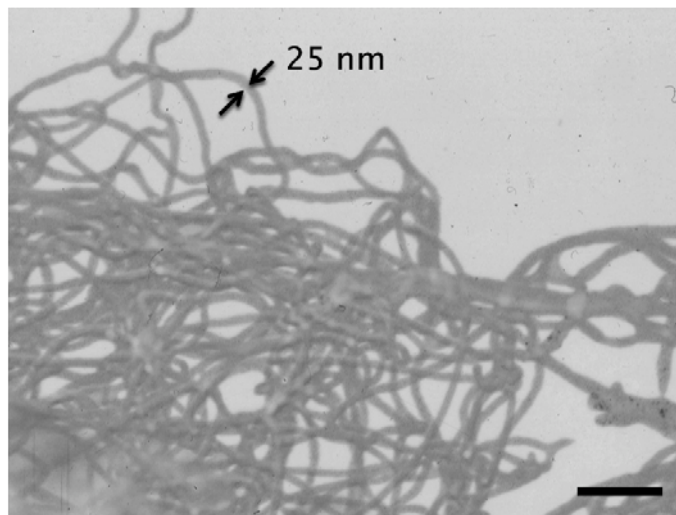


Figure 4.9: Low magnified dark field TEM image. The as-grown Sb nanowires have diameters in the range of 25 nm and lengths of a few  $\mu\text{m}$ . No crystalline features can be observed. Scale bar, 200 nm.

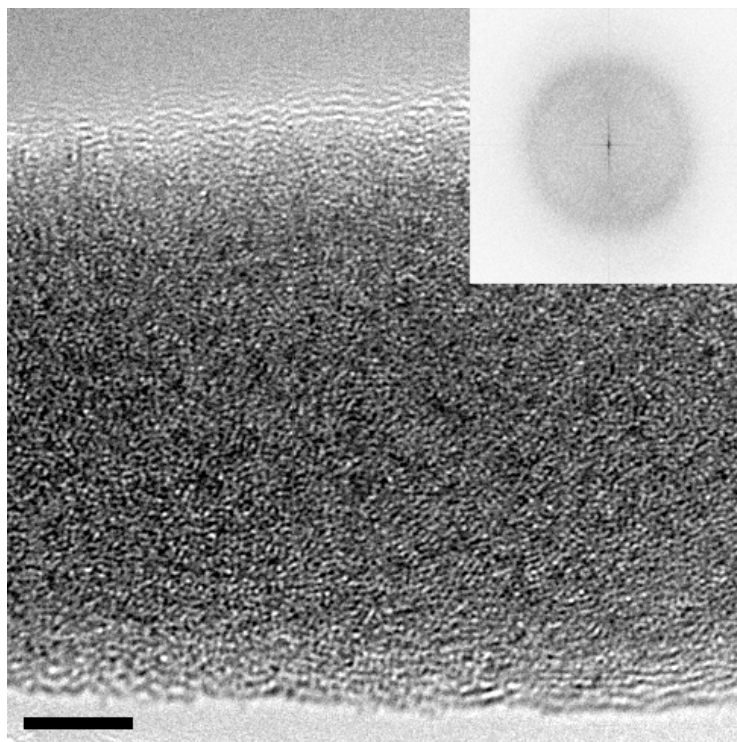


Figure 4.10: HRTEM image of a Sb nanowire in atomic resolution. The inserted SAED pattern proves the amorphous texture. The scale bar corresponds to 5 nm.

## 4.4 EDX Analysis of Sb Nanowires

The EDX tool equipped to the used HRTEM setup allows the investigation of individual nanowires. Fig. 4.11 shows the spectrum of a single nanowire. The nanowires appear to consist of pure Sb with traces of oxygen. These may result from a thin oxide layer surrounding the nanowire. The copper signal is an artefact originating from the TEM sample holder. Remarkably no Ga is detected, which was expected to originate from the FIB.

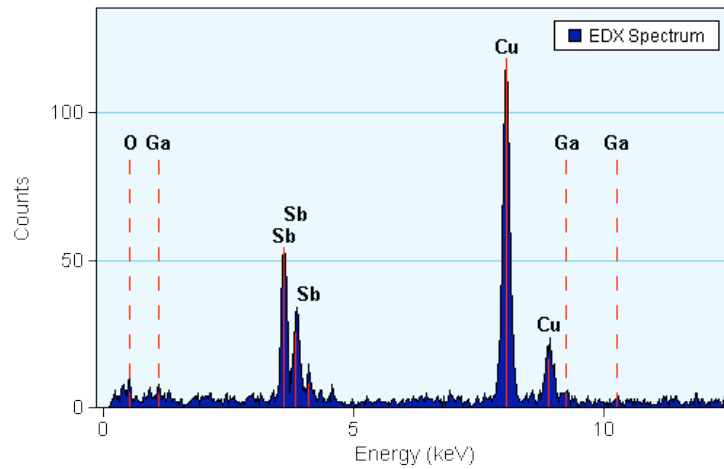
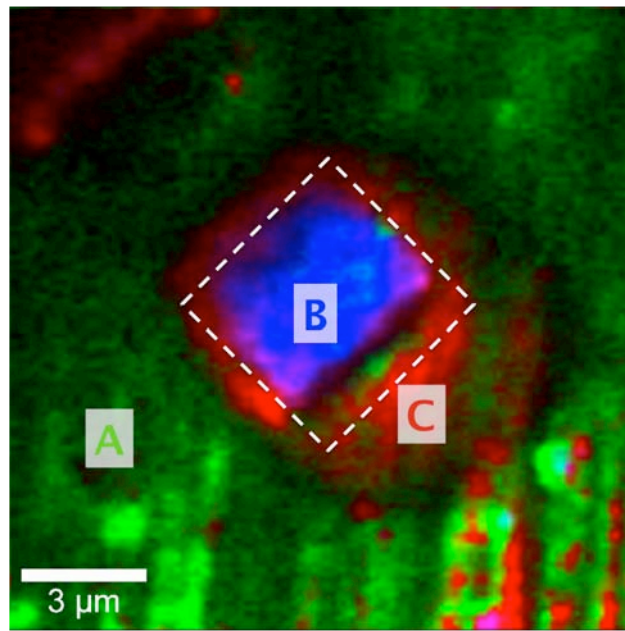


Figure 4.11: The graph shows the EDX spectrum of a single nanowire. The copper signal is an artifact from the TEM sample holder.

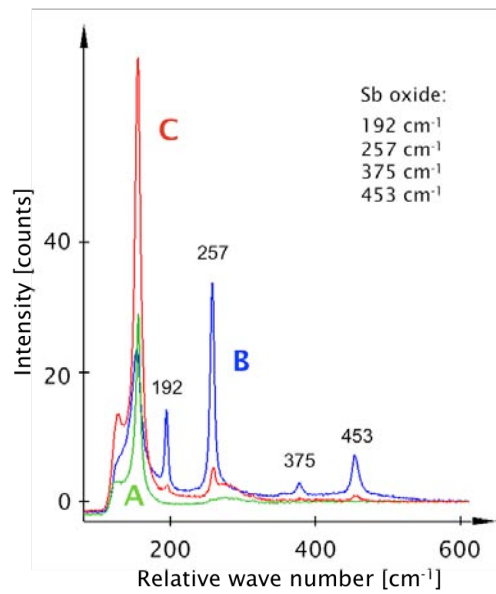
## 4.5 Raman Analysis of Sb Nanowires

A Raman scanning image of a FIB milled box is shown in Fig. 4.12(a). The Sb surface was exposed to an ion fluence of  $3.1 \times 10^{18}$  ions/cm<sup>2</sup>. The image is colored in a way that emphasizes the dominant part of the spectrum in Fig. 4.12(b). The green color surrounding the milled box is untreated Sb. The appropriate spectrum (green line) is in good coincidence with the Raman spectrum of pure Sb. The irradiated area is marked by the dashed rectangle and colored blue and red in the image. The spectra (blue and red line in Fig. 4.12(b)) differ from the pure Sb spectrum as additionally peaks appear. These peaks in both spectra at  $192\text{ cm}^{-1}$ ,  $257\text{ cm}^{-1}$ ,  $375\text{ cm}^{-1}$ , and  $453\text{ cm}^{-1}$  are identified as typical peaks for antimony oxide. The variation of the peak intensities results from a differences in the morphological structure of the antimony oxide. By this methode, the existence of an oxide species at ion exposed areas is clearly verified. It is assumed that the nanowires are surrounded by a thin oxide shell.





(a)



(b)

Figure 4.12: Color-coded Raman image of a  $(5 \times 5) \mu\text{m}^2$  FIB milled box (ion fluence of  $3,1 \times 10^{18}$  ions/cm<sup>2</sup>). The green area (denoted A) in the Raman image shown in (a) and the respective spectrum (A) in (b) proves the untreated surface to consist of pure antimony. The FIB milling box is marked by a dashed rectangle. Ion exposed areas are covered with nanowires and appear in blue and red color (denoted B and C, respectively). The according spectra (denoted B and C) show significant peaks at values corresponding to antimony oxide.

## 4.6 Mechanism of Sb Nanowire Growth

Even if the nanowire formation requires neither precursor gas nor enhanced temperature treatment, a model similar to the vapor-liquid-solid (VLS) growth mechanism is proposed. VLS was already discovered in the early seventies by Wagner and Ellis [37] and first theoretically treated by Givargizov [38] about ten years later.

VLS deals with the fact that a catalytic metal particle on the sample surface - if the ambient temperature is high enough - forms a liquid alloy cluster and serves as the preferential site for adsorption of reactant from the vapor phase.

The schematic in Fig. 4.13 shows exemplarily the VLS mechanism for the synthesis of Si nanowires using Au as catalyst. Au nanoparticles are deposited on a Si substrate (Fig. 4.13(a)) forming liquid alloy clusters when heated up to 500 °C. With introduction of silane (Fig. 4.13(b)), the molecules adsorbed at the catalytic alloy cluster are cracked into Si and 2H<sub>2</sub>. Molecular H<sub>2</sub> desorbs, whereas Si is solved in the droplet (Fig. 4.13(c)). With further absorption the concentration of Si exceeds saturation in the alloy droplet. This leads to precipitation of Si at the interface between the alloy cluster and the substrate surface, forming a crystalline nanowire (Fig. 4.13(d)). It is supposed that supersaturation is the driving force for nucleation of seeds at the interface between the catalytic alloy cluster and the substrate surface giving rise to a highly anisotropic growth of nanostructures. Nanowire growth continues as long as the droplet remains in a liquid state and supersaturation is maintained. This model is not solely limited to using Au as catalyst, it is also reported on various other metals such as Fe [39], Al [40], Ti [41], and also on Ga [42].

For a better understanding of the FIB induced growth mechanism, a growth model related to VLS is schematically shown in Fig. 4.14. We assume that FIB processing with the Ga beam (Fig. 4.14(a)) aside of sputtering produces mobile Ga species on the surface (Fig. 4.14(b)), which rapidly agglomerate forming liquid catalytic nanoclusters. Further sputtered Sb diffuses on the surface (Fig. 4.14(c)) and acts as material source. An excess of Sb easily leads to supersaturation of Sb in the catalyst droplet finally initiating the precipitation of the Sb nanowires (Fig. 4.14(d)) in form of loops beginning and ending in the droplet. As long as the droplet catalyst remains in a liquid state and supersaturation



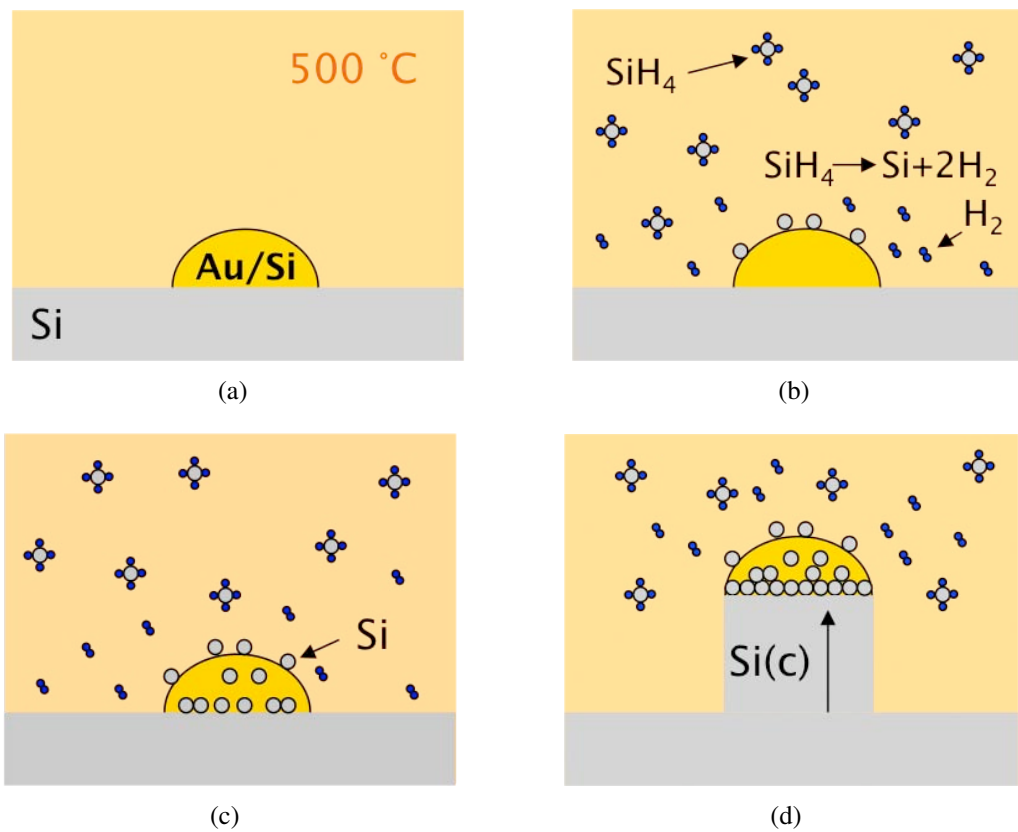


Figure 4.13: Schematic illustration of the VLS growth mechanism. Au nanoparticles deposited on Si are heated up to 500 °C forming a liquid droplet (a). Introduced silane molecules are adsorbed and cracked at the catalytic alloy cluster (b). Si is solved in the droplet (c). In case of supersaturation, a crystalline Si nanowire precipitates at the interface between the droplet and the Si substrate surface (d).

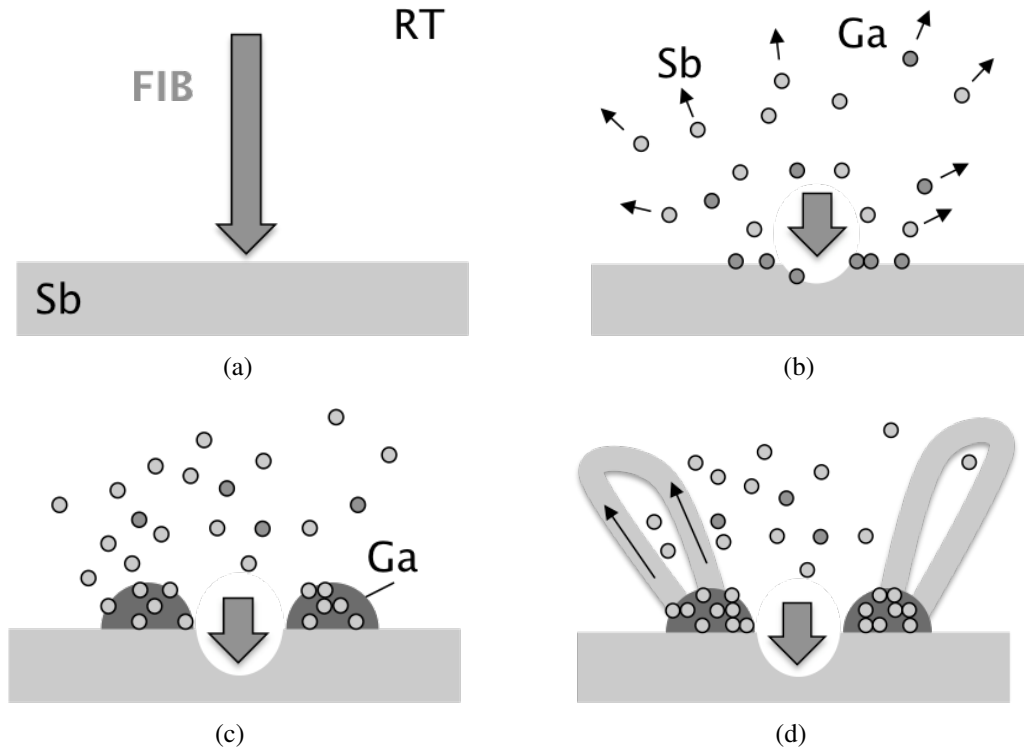


Figure 4.14: Schematic illustration of the proposed FIB based nanowire formation mechanism. The FIB impinges the Sb substrate at room temperature (a). The impact of the FIB results in sputtering of Sb clusters (b). Ga provided by the FIB rapidly agglomerates nearby FIB exposed sites forming Ga-rich nanoclusters (c). These act as preferential site for absorption of mobile Sb species and finally leads to supersaturation and precipitation of Sb nanowires (d).

due to subsequent delivery of sputtered Sb species is ensured the nanowires can continue to grow. The Ga catalyst is provided by the FIB itself and the sputtered substrate clusters may act as quasi-vapor material source for the growth of the nanostructures on and nearby the ion exposed area. At present, the origin of the tangling of the nanowires is not understood although extensive tangling has been reported previously in Ga based VLS processes [43]. The authors of [43] also stated that Ga droplets could simultaneously catalyze the growth of hundreds of thousands of nanowires. Additionally it has to be mentioned that in contrast to the conventional VLS mechanism the growth rate for the FIB based approach is extremely high. As the whole FIB processing takes only a few seconds, the growth rate has to be in the range of several 100 nm/s.

### 4.6.1 Key Parameters for Nanowire Formation with FIB

According to our experimental results, we assume that at least three essential key parameters are required to induce nanowire formation by an intense FIB:

- The coexistence of the liquid alloy nanocluster and the solid material has to be ensured.
- The substrate material has to feature a low melting liquid alloy with Ga.
- The energy entry by the FIB has to be high enough to keep the alloy in a liquid state.

Based on the proposed growth model in the following few sections these key parameters are discussed in more detail.

#### Phase Diagram of a Binary Ga-Sb System

The formation of pure Sb nanowires could be discussed by examining the Sb-rich part of the binary Ga-Sb phase diagram in Fig. 4.15. As stated in the growth model, FIB processing of the Sb substrate produces mobile Ga and Sb species on the surface that rapidly agglomerate forming liquid nanoclusters. With Sb substrates the only way to introduce Ga is supply by the FIB. The concentration of these clusters is assumed to be somewhere in the right-most part of the phase diagram, where the content of Sb is dominant. When the concentration of the solved materials exceeds supersaturation, nucleation sites will be formed. As a consequence, at these sites the growth of the coexisting pure Sb phase precipitating as nanowires is initiated. Nanowire growth from the base continues as long as the droplet remains in a liquid state and reactant is available. In accordance with the phase diagram precipitation of Sb continues at the liquid-solid interface as long as the catalytic particle remains in a liquid state and reactant is available. Even when FIB induced nanowire growth occurs far-off the thermodynamic equilibrium, known phase diagrams can be used to choose a specific composition (catalyst - nanowire material) so that there is coexistence of liquid alloy and solid material.

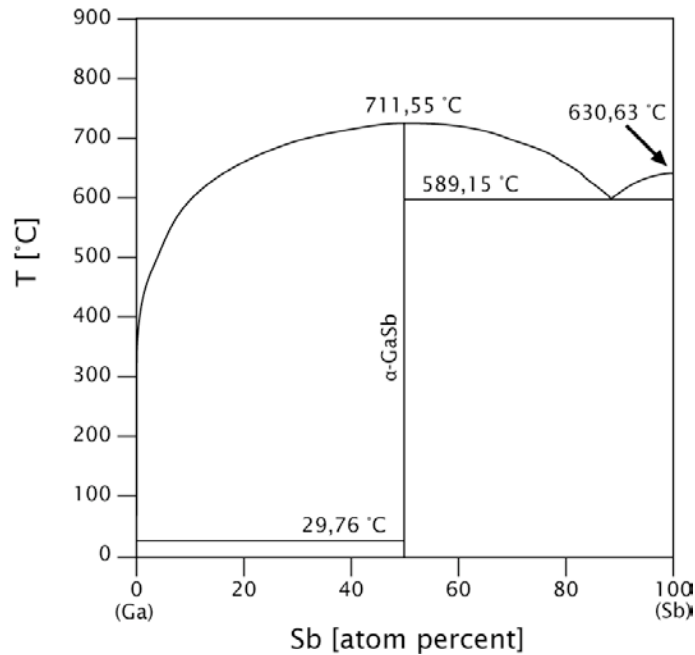


Figure 4.15: Binary phase diagram of Ga and Sb [44].

### Formation of Catalytic Nanocluster on Sb

The catalytic activity of Ga ions can be proved by variation of the ion species provided by the FIB. The FIB setup at the Research Center Dresden-Rossendorf allows the use of different liquid metal ion sources. For Sb samples exposed to 60 keV accelerated Si (Fig. 4.17) and Au ions (Fig. 4.16) hardly any nanowire formation was observed. Some nanostructure formation is observed with exposure to Si ions. It is suggested, that these nanostructures are not generated in a catalytic process but maybe in a point defect migration mechanism as observed for GaSb [35]. However, the melting point of Si at 1410 °C is much too high to form any kind of liquid alloy cluster needed for the catalytic growth of nanowires. Under the given experimental conditions the same applies for irradiation with Au ions. The melting point of 1064 °C is too high for liquid alloy cluster formation.

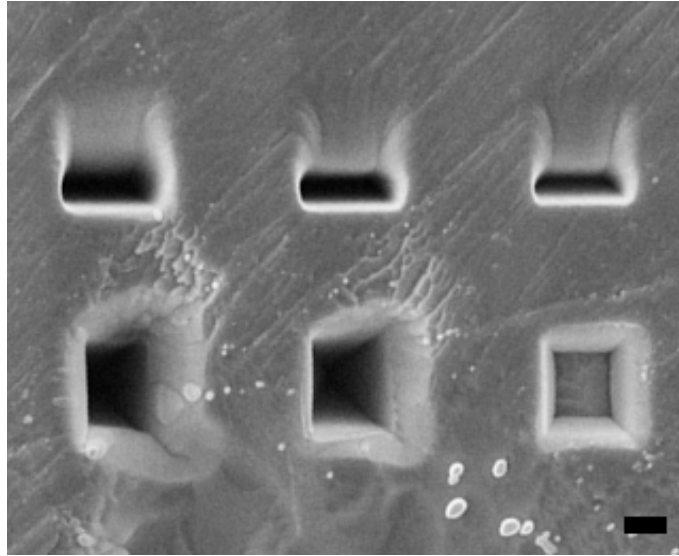
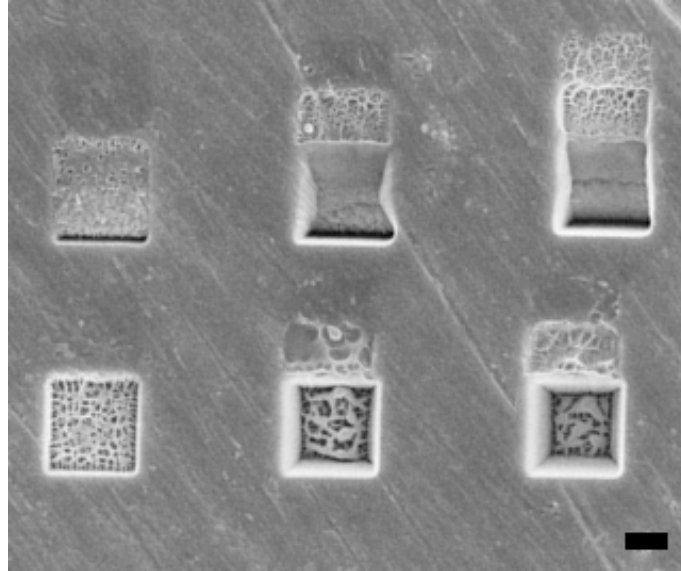


Figure 4.16: Sb substrate exposed to 60 keV Au ions in single pass mode (upper row) and multi pass mode varying from lower ( $F=6,2 \times 10^{17}$  ions/cm<sup>2</sup>) to higher ( $F=6,2 \times 10^{18}$  ions/cm<sup>2</sup>) ion fluences from right to left. No nanowire formation is observed. Scale bar, 1  $\mu$ m.

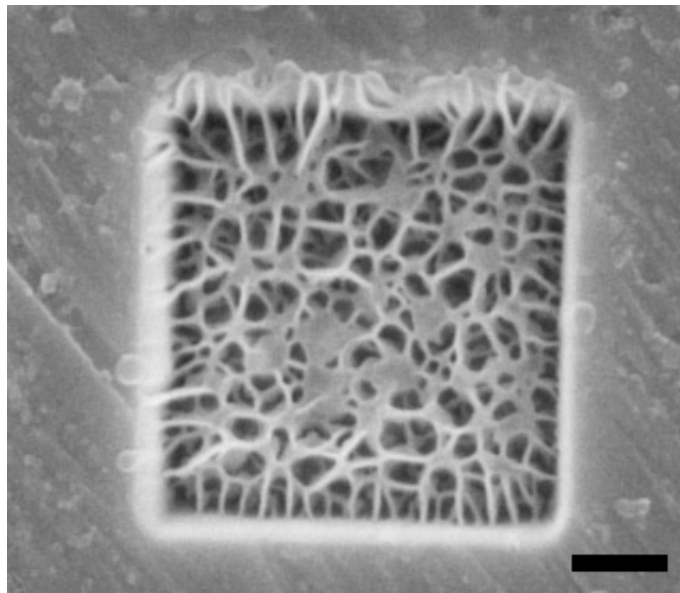
### Impact of Substrate Temperature on the Ga-Sb System

To investigate the influence of the substrate temperature, a set of experiments on Sb substrates exposed to a 30 keV Ga FIB with varying substrate temperature from  $-150$  °C to  $300$  °C was carried out. A special cryo-stage adapted for the FIB system at EMPA Dübendorf, Switzerland enabled this investigation. Significant reduction of nanowire growth is observed when the sample was cooled down to the minimum temperature of  $-150$  °C (Fig. 4.18). Lowering the ambient temperature seems to counteract the FIB induced local heating. The energy supply by the FIB may be too low to keep the catalyst in a liquid state as needed for the VLS-related nanowire growth process. Consequently, the Ga provided by the FIB agglomerates to droplet-like structures without any catalytic synthesis of nanowires.

For experiments carried out at temperatures above room temperature up to  $300$  °C the phenomenon of reduced nanowire growth is observed too. Thereby, the Sb substrates were irradiated by a 30 keV Ga FIB system installed at the Research Center Dresden-Rossendorf, Germany that allowed heating up the sample while processing. Hardly any



(a)



(b)

Figure 4.17: Sb substrate exposed to 60 keV Si ions. In (a) FIB processing is performed in single pass mode (upper row) and multi pass mode varying from lower ( $F=6,2\times 10^{17}$  ions/cm<sup>2</sup>) to higher ( $F=6,2\times 10^{18}$  ions/cm<sup>2</sup>) ion fluences from left to right. Scale bar, 1  $\mu\text{m}$ . The close-up view of a  $(2\times 2)$   $\mu\text{m}^2$  multi pass milled box ( $F=6,2\times 10^{17}$  ions/cm<sup>2</sup>) in (b) shows in more detail the resulting network structure due to point defect. Scale bar, 500 nm.

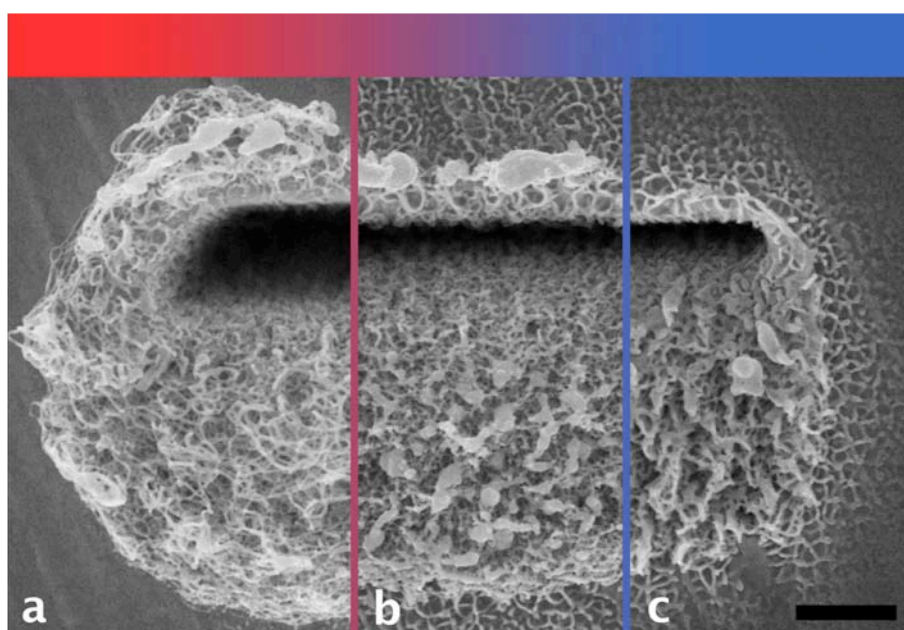


Figure 4.18: SEM images of Sb exposed to the 30 keV Ga FIB at (a) 0 °C, (b) –100 °C and (c) –150 °C. The FIB processing of samples cooled by liquid nitrogen leads to significant reduction of the density of the nanowire network. Scale bar, 500 nm.

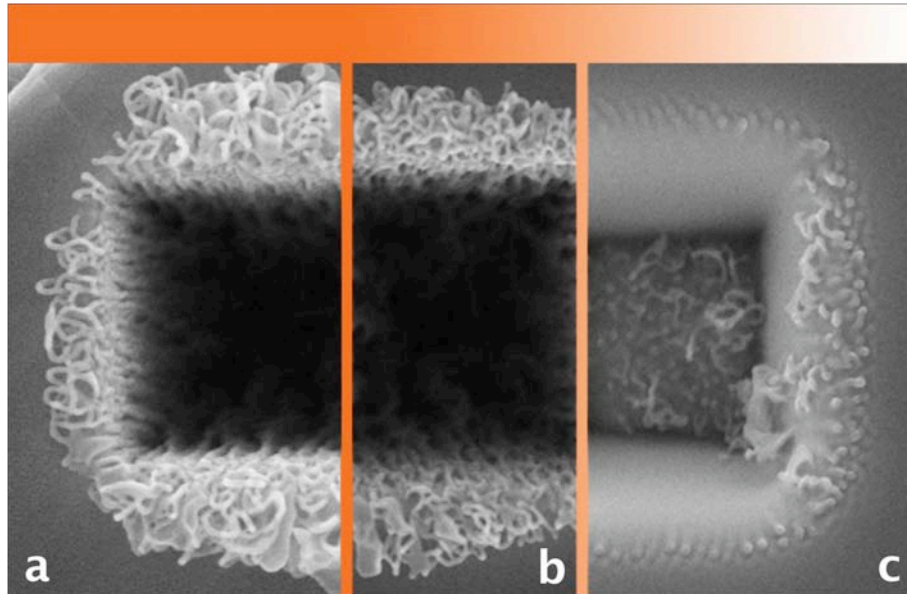


Figure 4.19: Sb substrates exposed to the Ga FIB with (a) 50 keV, (b) 30 keV and (c) 10 keV.

nanowire formation is observed at temperatures of 150 °C and 300 °C.

Additional experiments were carried out at different beam energies. With a decrease in ion energy a decrease of the nanowire density is observed. The beam energy might be too low to ensure the formation of a liquid alloy luster during the FIB process. SEM images of Sb substrates exposed to 50 keV, 30 keV and 10 keV Ga ions are shown in Fig. 4.19.

We showed that the process temperature is a crucial parameter. At temperatures below room temperature the resulting nanostructures on Sb exposed to the Ga FIB look similar to those generated on GaSb. Investigation on substrates FIB processed at temperature beyond +150 °C also leads to reduction of nanowire growth. Therefore the processing window seems to be very small. Especially melting temperature and thermal conductivity seem to play an important role for the suggested growth model. Tab. 4.1 gives an overview list of investigated substrates and their thermodynamic properties. Nanowire synthesis is only observed with materials all having melting points between 600 °C and 1000 °C and a comparable low thermal conductivity. Both parameters have to be in the ideal range for nanowire growth. Although InAs according to the listed values for melting point



Material	Melting point [°C]	Therm. cond. [W/(m·K)]	
Ga	30	29	
In	157	82	
Sn	232	85	
Bi	271	7,87	
Tl	304	46,1	
Pb	327	35,3	
Zn	419	132	
Te	450	2,35	
InSb	525	18	
Sb	631	24	
Mg	649	156	
GaSb	712	32	
InAs	942	27	
Ge	958	58	
Ag	961	406	
Au	1064	345	
GaAs	1240	55	
Si	1412	130	
Ni	1455	158	
GaP	1477	110	

**melting point  
too low**

**growth of nanowires**

**melting point  
too high**

Table 4.1: Investigated materials with melting point and thermal conductivity.

and thermal conductivity would fulfill these requirement no nanowire growth with FIB exposure is observed. This could be explained by decomposition of InAs and the high volatility of As. The formation of In crystallites instead has already been discussed in a former chapter.

## 4.7 Recrystallization of Sb Nanowires

As shown by HRTEM and SAED analysis the as-grown Sb nanowires consist of pure Sb and are amorphous. Barati et al. reported that amorphous regions in Sb nanowires electrodeposited in porous anodic aluminum discs can be re-crystallized by a post-annealing process at temperatures of about 150 °C [45].

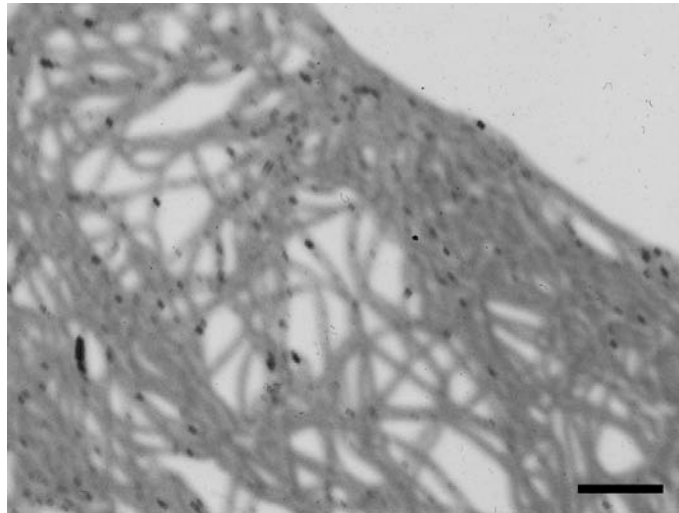


Figure 4.20: Dark field TEM image of Sb nanowires after annealing at 180 °C for 30 min in He. As this special TEM technique allows visualization of crystalline regions of a selected crystallographic orientation, grains which contribute to the chosen orientation can be recognized as black dots. Their sizes are in the order of the wire diameter. Scale bar, 200 nm.

To recrystallize the Sb nanowires, the FIB modified samples covered by the nanowires were annealed in a special furnace setup which allows processing at well-controlled temperature profiles in He atmosphere. Annealing at 180 °C for 30 min leads to recrystallization of the initial amorphous Sb nanowires. The diameter and shape of the nanowires remain unaffected by this annealing process. The formation of crystalline grains very homogeneous in size are observed. In the inverted dark field TEM image in Fig. 4.20 crystallites with common crystallographic orientation appear as black dots. The diameters of crystallites are usually in the range of the nanowire diameter. The HRTEM image in Fig. 4.21 displays a Sb nanowire after moderate thermal annealing at 180 °C for 30 min, the according diffraction pattern in the inset shows the most prominent (110) and (120) reflections for Sb with its trigonal crystal structure. The lattice parameter of 0,354 nm is consistent with the tabulated value for bulk Sb [46].

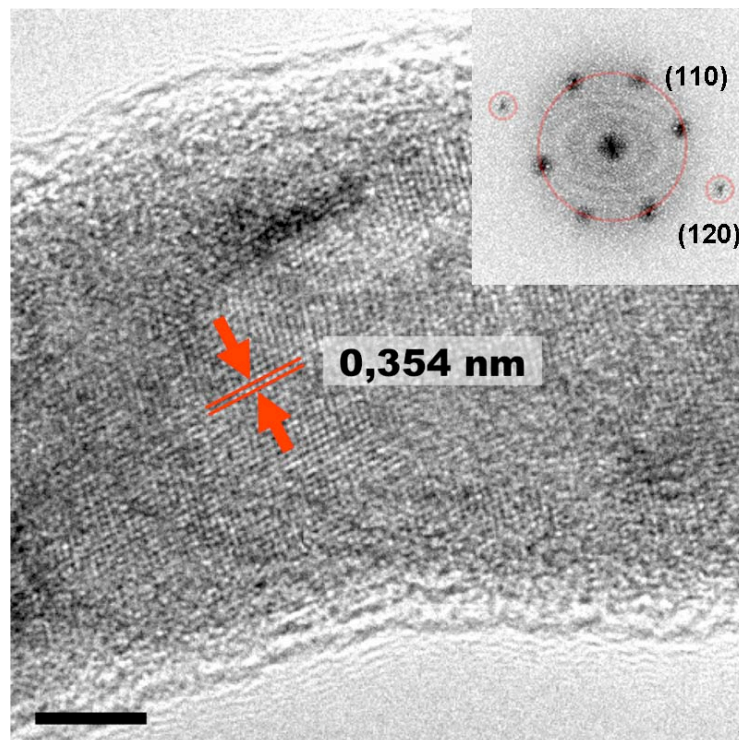


Figure 4.21: HRTEM micrograph of a part of a Sb nanowire after thermal annealing at 180 °C for 30 min in He. The lattice planes as highlighted in the HRTEM image show a distance of 0,354 nm which corresponds to Sb (110) direction. The inserted SAED pattern clearly shows the single crystalline nature ((110) and (120) reflections) of the nanowires after the post growth annealing. The scale bar corresponds to 5 nm.

## **Chapter 5**

# **Electrical Characterization**

### **5.1 Device Fabrication and Electrical Characterization**

#### **5.1.1 Contacting a Single Sb Nanowire**

To investigate the electrical properties of the FIB generated Sb nanowires, they have to be separated from the Sb surface and transferred onto an isolating substrate for further processing of contact electrodes. The complete process flow of contacting nanowires is given in Fig. 5.1. The carrier substrates are pieces of a Si (111) wafer covered with a 200 nm thick layer of SiO<sub>2</sub>. Optical lithography is used for preparing marker structures for all following electron beam lithography (EBL) alignment steps.

For the transfer of the Sb nanowires, the uplifting effect of the FIB generated nanostructures, which can be observed under certain process conditions, is a big advantage. By simply pressing the Sb sample upside-down onto a piece of the carrier substrate, the nanowires break off and some of them remain on the isolating surface. Well-separated Sb nanowires, which are suitable to be contacted by metal electrodes are detected by SEM imaging.

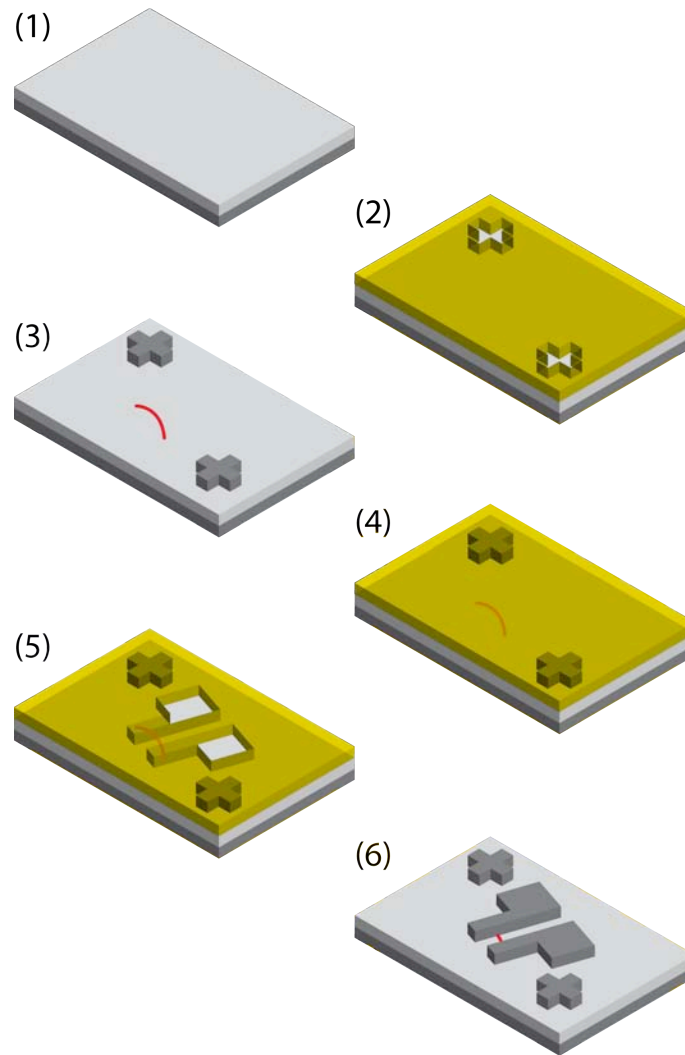


Figure 5.1: The 3D illustration shows the process flow of making contacts to nanowires: (1) covering of Si substrate with  $\text{SiO}_2$  layer, (2) formation of marker structures for EBL, (3) transfer of the Sb nanowires (here indicated as red line) onto the substrate surface, (4) PMMA coating for EBL exposure, (5) development, (6) metallization with Ti and Au and lift-off process. The contacted Sb nanowire is ready for measurement.

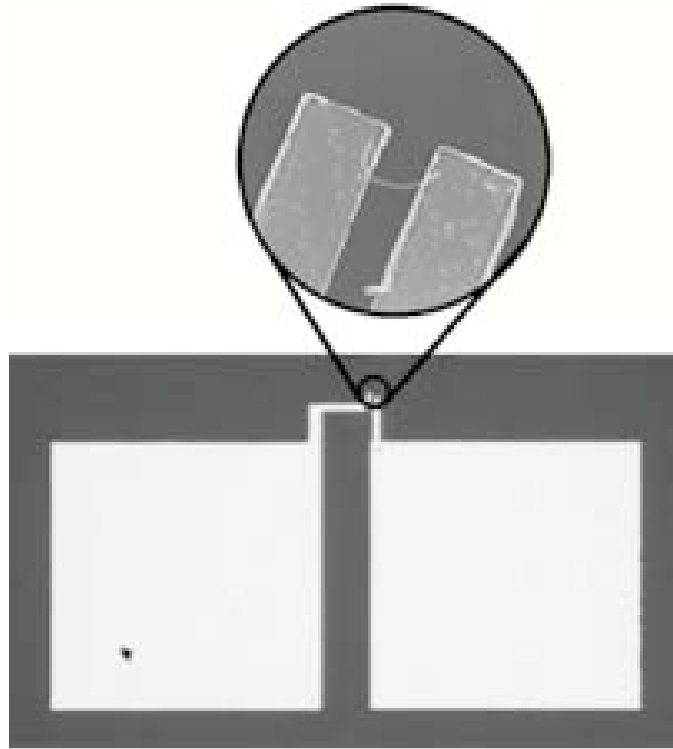


Figure 5.2: Optical microscopy image of the contact pattern and the enlarged view (SEM) of the Sb nanowire contacted to the Ti/Au fingers.

The as-grown Sb nanowires on the Sb substrate show lengths up to some micrometers. With the mechanical cut-down and transfer of the nanowires in this rather ungentle way they break several times. Therefore the observed sizes of the nanowire fragments on the carrier substrate are only in the submicron range. The use of SEM and EBL is a practicable method to process high-resolution patterns, which are essential for the fabrication of metallic electrodes contacting the nanowire. For the processing of these pads, first of all the exact positions of the nanowires in correlation to the marker structures has to be specified in the EBL setup. After spin coating with PMMA - a special electron sensitive resist - the sample is introduced into the EBL setup again. Accurate alignment of the marker structure has to be performed before starting the exposure process. Individually designed patterns forming the electrode structures can now be transferred onto the resist-coated sample. After development Ti/Au layers are sputter deposited. A following lift-off process results in the electrode structures. The SEM close-up view in Fig. 5.2 shows the

Sb nanowire fragment contacted by two electrode fingers. The large Ti/Au pads visible in the optical microscopy image measure  $(120 \times 120) \mu\text{m}^2$  enabling to position the tungsten needles with micromanipulators in the prober station. These sharp needles ensure a reliable electrical contact for measurement.

## 5.2 Electrical Characterization of a Single Sb Nanowire

The FIB generated Sb nanowires show diameters of about 25 nm. It is obvious, that a current flowing through such a nanowire is expected to be in the fA to nA regime. To be able to measure such small current special equipment is needed. We use a sample prober station from SUSS MicroTec with tungsten needles mounted on micromanipulators to place each of the needles individually on the corresponding contact pad. Triaxial cables connect this setup to a HP 4156B Semiconductor Analyzer, which allows force and sensing of currents in the low pA regime.

It is of great interest to gain more information on the conductivity behavior of nanostructures as they are suggested to have unique electrical properties. An ideal way to do resistance measurement is the so-called 4-terminal sensing [47]. Thereby measurement of the contact resistance is avoided. The Sb nanowire fragments with lengths of several 100 nm are too small to place four separated electrodes on one single nanowire. Therefore we have to get along with 2-point-measurements although this method gives only an upper limit for the nanowire resistance. It does not provide an insight into the distribution of the total measured resistance value in shares for contact and actual resistance of the nanowire itself.

All investigations were carried out under well-defined conditions in a special test rig equipped with a closed chamber. To perform I/V characterization with this measurement equipment the sample had to be slightly modified. The setup in a vacuum chamber requires that the contact pads are connected to edgeboard contacts on an epoxy plate achieved by Au wire bonding. As wire bonding requires thermopressing at moderate temperature, thicker and larger metal pads to endure these conditions are processed by optical lithography. In a subsequent step, they are connected with the Sb nanowire by means of

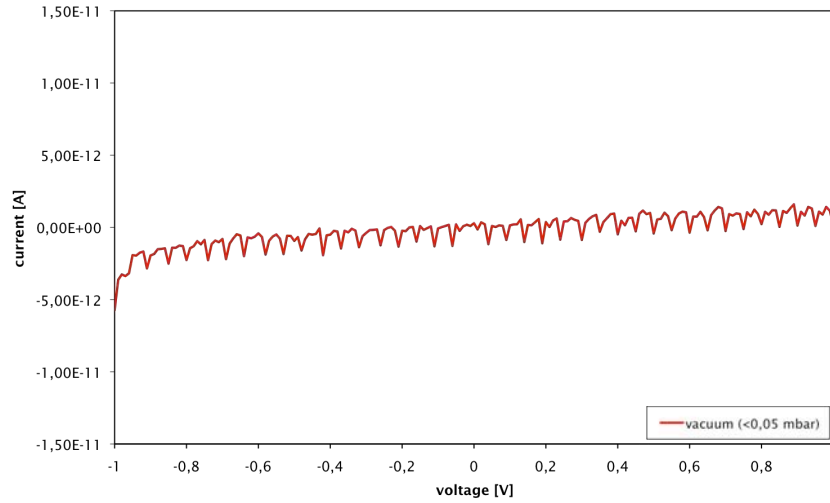


Figure 5.3: I/V characteristic for a FIB generated Sb nanowire in vacuum.

electron beam lithography (EBL). Metallization exclusively processed with EBL is too thin. The electrode pads would be destroyed during the wire bonding procedure. The copper contacts on the epoxy plate were linked to cables guiding to an electrode feedthrough and further route the measurement signal via shielded cables to the analyzer. By that change in the setup, it was feasible to reproduce the results. For better control of the ambient atmosphere inside the chamber, the vacuum chamber was connected to a pump system offering the possibility to measure under high-vacuum conditions.

The curve in Fig. 5.3 shows the I/V curve of a single Sb nanowire under vacuum conditions (pressure of residual gas:  $< 0,05$  mbar). The remarkable noise is attributed to the rather low measured currents due to the high ohmic resistance of the device, which is estimated to be at least at values higher than 100 GOhm (including contact resistances). All these measurements in vacuum are close to the detection limit of the analyzer. Therefore, these values can only be considered as an upper bound of the actual resistance. Various tested Sb nanowire devices give all very similar results. To check this doubt we carried out additional measurement on isolated pads not connect by a nanowire, which resulted in an exact zero line.



	<b>Sb (bulk)</b>	<b>Sb (FIB-NW)</b>
spec. res. $\rho$	$3,9 \times 10^{-7} \Omega \cdot \text{m}$	$> 4,0 \times 10^2 \Omega \cdot \text{m}$
el. cond. $\sigma$	$2,6 \times 10^6 \text{ S/m}$	$< 2,5 \times 10^{-3} \text{ S/m}$

Table 5.1: Comparison of specific resistance  $\rho$  and electrical conductivity  $\sigma$  of both bulk Sb [48] and FIB synthesized Sb nanowires contacted with Ti/Au pads.

The measured resistivity values of the whole Sb nanowire device (not accounting the contribution of the contact patterns to the total resistance) converted into specific resistance and electrical conductivity, respectively, is given in Tab. 5.1. Compared to bulk properties known from literature [48] the values of specific resistance and electrical conductivity differ by nine orders of magnitude.

### 5.3 Sensing Properties

With samples and setup modified for measurements in vacuum chamber, it is also possible to check the impact of the ambient atmosphere. Several gases can be introduced in the measurement chamber. No influence on the conducting behavior of the nanowire was observed at the presence of  $\text{H}_2$ , He,  $\text{O}_2$ , and CO in the chamber. In Fig. 5.4 the appropriate I/V curves for (a) vacuum, (b) 100 mbar  $\text{O}_2$  and (c) 20 mbar CO, respectively, are illustrated. Especially the fact, that there is no response to CO is surprising as many solid-state sensors show a change in conductivity when exposed to reducing agents. With exposure to  $\text{H}_2$  and He the characteristic of the device shows an analogous curve like to that in vacuum,  $\text{O}_2$  or CO ambient. The supply of water or ethanol vapor, however, results in a significant change of the conduction depending on the respective concentration.

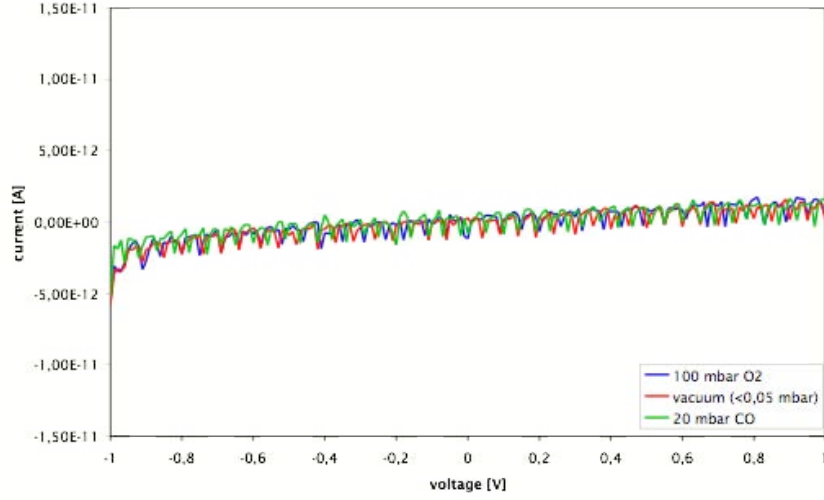


Figure 5.4: I/V characteristic for a FIB generated Sb nanowire measured (a) in vacuum, (b) in O<sub>2</sub> and (c) in CO. No impact due to the introduction of the gases is observed.

### 5.3.1 Sb Nanowire Response to Water Vapor

Fig. 5.5 shows the I/V characteristic of the Sb nanowire device for various pressures of water vapor as given in the legend. The I/V diagrams show that the Sb nanowire device changes its conductivity in response to changes in gas concentration and thus provides information about the ambient environment.

A well-established parameter for a sensor is the so-called sensitivity. This value gives the increment factor of the conductivity through the nanowire device in units of the initial current measured under vacuum conditions. The sensitivity or gas response of the nanowire sensor is therefore calculated as the ratio between  $R_0$  (the resistance of the device measured in the vacuum ambient) and  $R_g$  (defined as the resistance when the sensor is exposed to a certain amount of gas),

$$S = \frac{R_0}{R_g}. \quad (5.1)$$

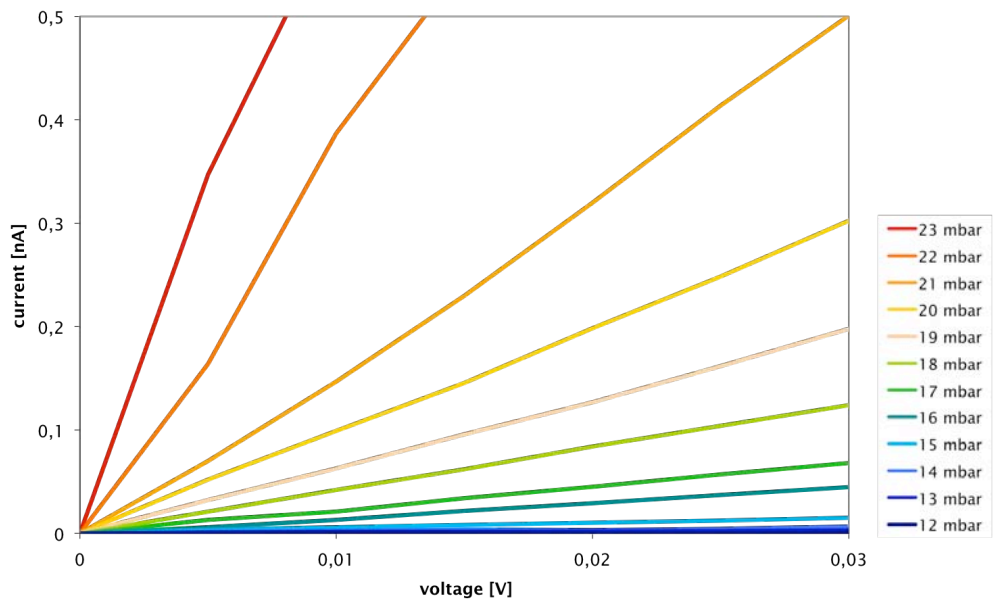


Figure 5.5: Plot of I/V characteristics of the Sb nanowire device as a function of the partial pressure of water.

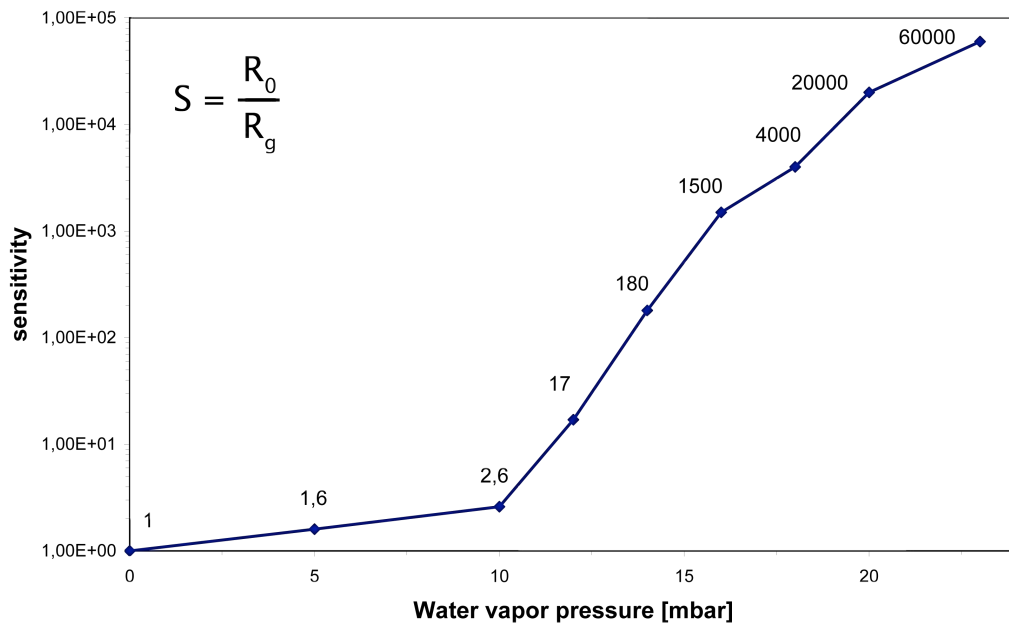


Figure 5.6: Sensitivity of the Sb nanowire sensor device exposed to water vapor as a function of pressure.

Thus, a much better visualization of the sensing properties and comparability with other sensing systems is achieved. Plotting the sensitivity as a function of pressure shows the sensing effect in dependence on the amount of gas introduced into the chamber.

Sensing properties are often checked in synthetic air (SA) ambient, which is a mixture of 4:1 of  $N_2$  and  $O_2$ . For sensing the gas is just added proportional using SA as carrier. Some differences of the sensitivity of the nanowire device are probably when measuring in SA instead of in vacuum ambient due to the fact, that adsorption of oxygen and nitrogen molecules and the other introduced of gas molecules are competing processes. Therefore our Sb nanowire device might show lower sensitivity in SA ambient. However, especially the irreproducible results of the very first experiments most probably due to varying content of humidity in the ambient air prove the sensing effect of our Sb nanowire also under atmospheric conditions.

The characteristic of the sensitivity value rising with water vapor pressure observed in the graph in Fig. 5.6 is quite interesting. Whereas at low partial pressures only a low increase is observed, above 10 mbar the sensitivity value increases rapidly. Starting predefined at an initial sensitivity value of 1 at 0% the sensitivity marginally increases to 2,6 as the water pressure is increased to 10 mbar, which already corresponds to a relative humidity of about 40%. Further increase of the water pressure in the chamber leads to a nearly exponentially increase of the sensitivity values of 17 at 12 mbar, 1500 at 16 mbar and finally 60000 at the maximum vapor pressure of 24 mbar.

### 5.3.2 Sb Nanowire Response to Ethanol Vapor

Introduction of ethanol vapor shows sensing properties analogous to those observed for water vapor. Fig. 5.7 gives the I/V characteristic of the Sb nanowire device for various pressures of ethanol vapor as given in the legend.

The curve in Fig. 5.8 visualizes the sensing potential for ethanol. As for water vapor the sensitivity increases by more than four orders of magnitude depending on the introduced gas amount. Starting at low pressures of below 10% of the ethanol vapor pressure the sensitivity is in the range of 1 to 1,25 steadily raising to a value of 30 at an ethanol

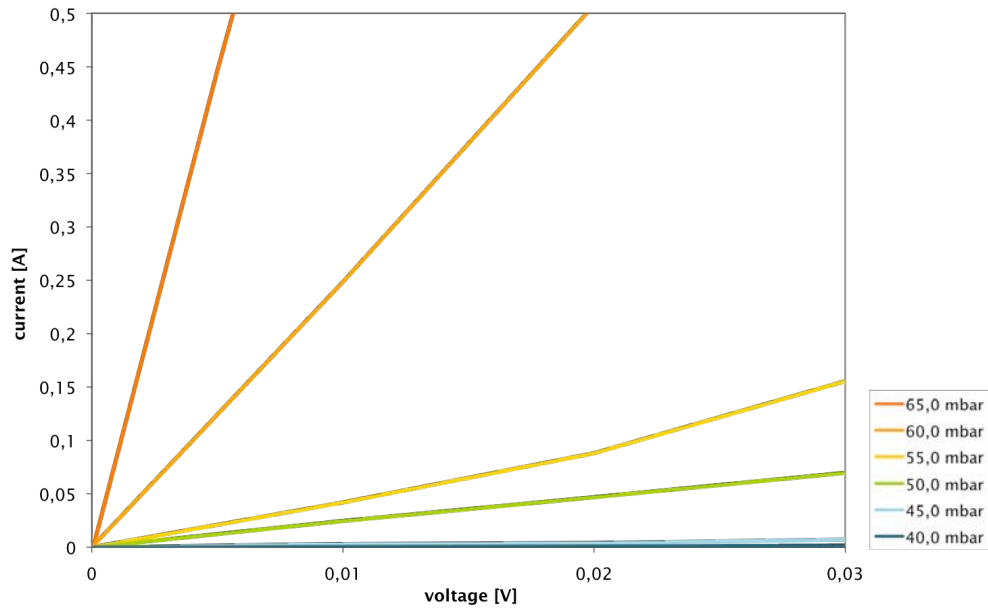


Figure 5.7: I/V characteristics of Sb nanowire exposed to ethanol vapor.

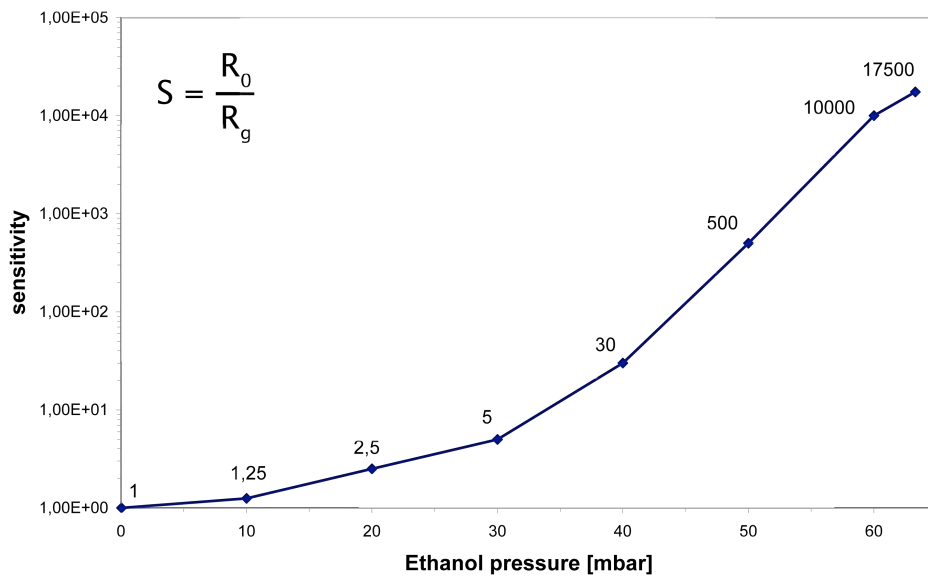


Figure 5.8: Sensitivity of the Sb nanowire sensor device exposed to ethanol vapor as a function of pressure.

pressure of 40 mbar and finally appreciating to a sensitivity of more than 10000 at the maximum ethanol vapor pressure of 65 mbar at a temperature of 22 °C.

## 5.4 Response and Recovery Time of the Sb Nanowire in Ethanol Vapor

Sensors are not only characterized by sensitivity, parameters such as the response and recovery time are of great interest concerning their practicable use. When a sensor is exposed to gas, it does not change its state immediately. The change to the new state lasts a period of time, called the response time. For recovery of a just gas exposed sensor to reach its (initial) state in absence of the gas again, this period of time is called recovery time.

The response and recovery characteristics of the Sb nanowire device exposed to 43,7 mbar ethanol, which corresponds to about 66% of maximum vapor pressure, are given in Fig. 5.9. When the current measurement starts the climate chamber is evacuated ( $p < 0,05$  mbar). The initial current at a fixed voltage of 1 V is about 5 pA. After 60 seconds (1) the initially evacuated chamber is vented by opening a valve to a reservoir filled with ethanol vapor. Thus, it is assured that the introduced gas penetrates the chamber volume immediately. In the following couple of minutes the response of the sensor is monitored. After about 9 minutes the sensor has reached the maximum sensitivity value. The current has reached its maximum of 150 pA, which is in good agreement with the expected current corresponding to the set ethanol pressure. Another valve to an already evacuated reservoir connected to a vacuum pump system is opened, so that the chamber pressure is exhausted in a few seconds to a final pressure below 0,1 mbar. After several minutes the initial sensitivity value of 1 is reached again. The current is reduced to its initial state of 5 pA again. A complete cycle of response and recovery is finished within 20 minutes. As this sensing procedure is completely reversible, the next cycle could start at once.

The observed response and recovery time of the sensor each lasting a couple of minutes is not an outstanding performance for a sensor but it has to be mentioned that our

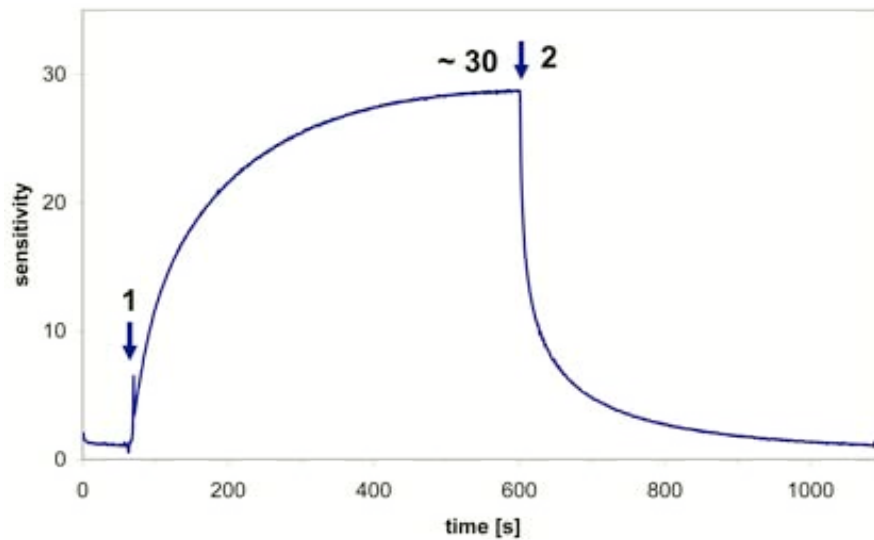


Figure 5.9: Response and recovery characteristics of the Sb nanowire sensor for ethanol: (1) Introduction of ethanol (43,7 mbar), (2) fast removal of the ethanol vapor by pumping to base pressure of about 0,05 mbar.

device is investigated at room temperature. Sensors are often characterized at operating temperature between 100 and 500 °C, which also might result in faster response and recovery times for our Sb nanowire sensor as adsorption and desorption are temperature dependent processes.

## Chapter 6

# Sensing Mechanism

### 6.1 Metal Oxide based Gas Sensors

Semiconductor gas sensors monitor changes in the conductance during the interaction of a chemical sensitive material with molecules to be detected in the gas phase. A huge variety of ceramic, thick-film, thin-film and nanowire based devices has been developed over the last decades. Investigation and analysis of their sensing properties often follow empirical studies and development work, the fundamental understanding of the sensing mechanism is rather poor [49, 50]. Generally, metal oxides have attracted great attention as they offer the opportunity of gas sensing under atmospheric conditions. The operation of these sensors mostly bases on materials such as  $\text{SnO}_2$ [7, 8, 50],  $\text{In}_2\text{O}_3$ [51, 52],  $\text{ZnSnO}_3$ [53, 54],  $\text{CeO}_2$ [55],  $\text{WO}_3$ [56],  $\text{MnWO}_4$ [57],  $\text{TiO}_2$ [58, 59],  $\text{Ga}_2\text{O}_3$ [60], and  $\text{Sb}_2\text{O}_3$ [60, 61]. For sensing, the conductance of the device is monitored as a function of the concentration of the target gas. The impact of the gas on the conductivity of the sensor material is transduced into electrical signals as the resistance of the sensing layer exposed to gas changes. The sensing itself takes place at different sites of the structure depending on the morphological structure of the layer [50]. Just to cite an example, compact and porous layers of one and the same material lead to completely different results. In the case of compact layers, the gas cannot penetrate into the sensitive layer, the interaction is only taking place at the outer geometric surface. With porous layers instead, the gas penetrates



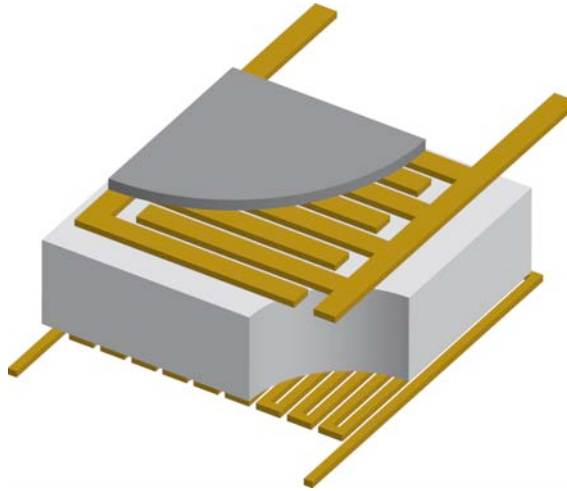


Figure 6.1: Schematic of a conventional solid state sensor device. Pt electrodes are processed on both, top and bottom side of a ceramics substrate, the top electrodes are then covered by the sensitive layer (e.g.  $\text{SnO}_2$ ) and therefore provide the electrical contact to the sensor material. The bottom electrodes are used to heat the whole setup to the desired operating temperature.

into the sensitive layer down to the interface with the substrate. Interaction with the gas therefore may happen at the surface of individual grains, at grain-grain boundaries and at the interface between grains and electrodes and grains and substrate. Basically, the difference is the total surface area that is affected by the target gas.

Conventional sensors are 2D layers of sensitive material deposited on electrode arrays. The schematic in Fig. 6.1 shows the complete device with a sensitive layer deposited on an isolating substrate provided with electrodes for the electrical measurements. Additional electrodes on the back of the substrate allow heating of the whole device to keep the sensor at a defined operational temperature. The choice of this temperature depends on the sensor material and the gas to be detected. Usually the sensors are operated at temperatures varying from 100 - 500 °C. Anyway, few sensors are also used at room temperature, e.g. the  $\text{CeO}_2$  based humidity sensors reported in [55].

Very recently, one-dimensional nanostructures such as nanowires and nanotubes have more and more attracted attention in the sensor community as their high surface to volume ratio makes them potential candidates to significantly improve the sensitivity of gas sensors.

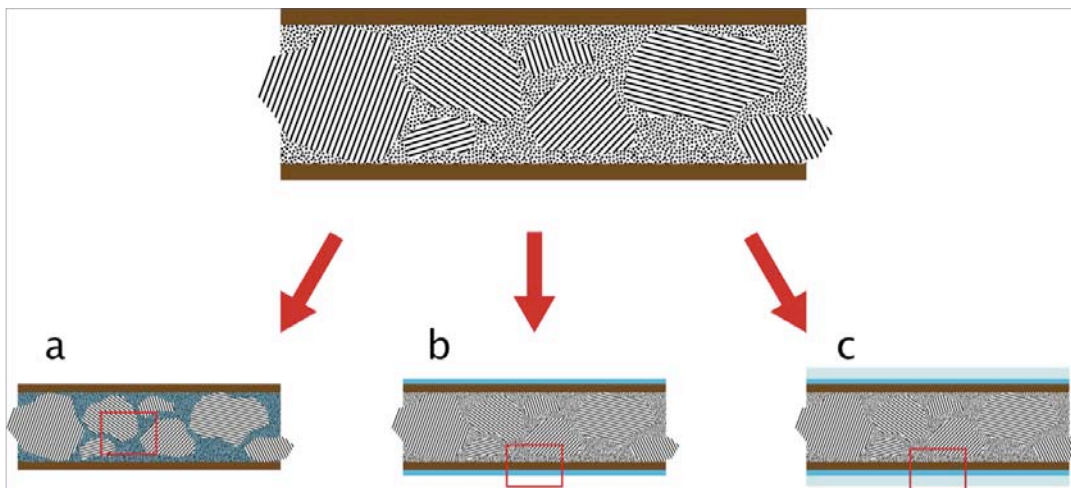


Figure 6.2: Schematic drawing to different sensing mechanisms. There are three possible ways (indicated by the red rectangles) for charge carriers to flow through the nanowire: (a) the nanowire core itself, (b) the metal oxide shell electrically modified by a chemisorbed layer, or (c) the adsorbed layers surrounding the nanowire.

## 6.2 Discussion of Sensing Mechanism

The main interest is to find an explanation for the sensing properties observed for Sb nanowires reported in the last chapter. For this purpose, some ideas of already existing theories on different sensing materials describing sensing behavior of thick-films, thin-films and nanowire structures are to be taken into account. They are then compared to the phenomena observed with the Sb nanowire devices and finally it is tried to find a reasonable interpretation finally leading to the right sensing mechanism.

In principle, the conduction of the Sb nanowire device has to occur through the nanowire core itself, the metal oxide shell, the adsorbed layers surrounding the nanowire, or a combination thereof (see Fig. 6.2). TEM investigation proves the morphological structure of a single Sb nanowire, which can be considered to be built up like a chain of nanocrystallites embedded in an amorphous region and covered by a thin oxide layer.

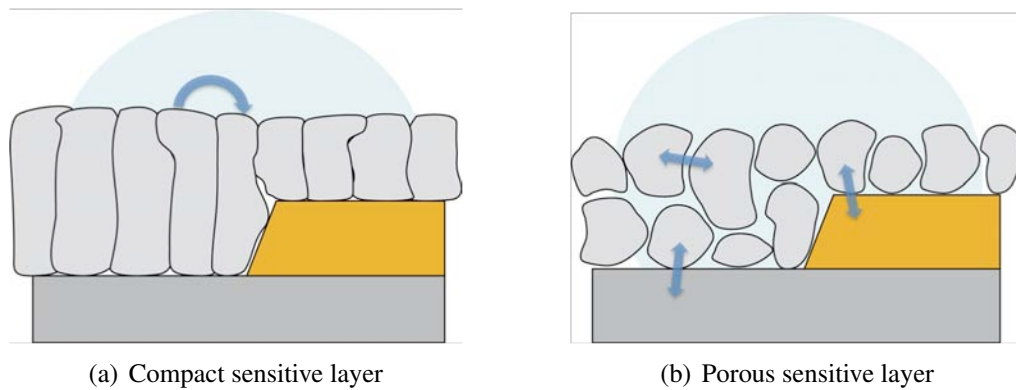


Figure 6.3: Different structures lead to different sensing capabilities. Whereas for compact sensor layers the gas only interacts with the surface of the sensitive layer, with porous materials additionally interaction between grains and electrodes and grains and substrates may occur therefore leading to a different result.

In the following the most likely currents paths through the Sb nanowire are discussed in more detail. After this discussion the actual sensing mechanism of the Sb nanowire device should be figured out.

### 6.2.1 Grain Boundary Barrier Modulation

Generally, the morphology and crystallinity of the sensitive layer play a decisive role on the conducting behavior. It is obvious that the resistance of compact layers compared to these of porous or grained structures differs, e.g. due to the presence of necks between grains providing insufficient conductivity. These necks act as boundary barriers and might be seen as a disadvantage of substructured materials at first glance. But from another point of view this fact offers great potential for sensing as the volume of porous layers is accessible to gases and the actual active sensor surface is much higher than for compact layers. This means that adsorption of gases may result in an increase as well as in a decrease of the resistance of the sensitive layer depending on the impact of the adsorption on the conductivity of the surface itself on the one hand and on grain boundary barrier modulation due to interaction of grains and size variation of necks on the other hand. Fig. 6.3 illustrates the differences between compact and porous layer. Whereas the adsorption of gas can only take place on the geometric surface with compact structures, for porous layers

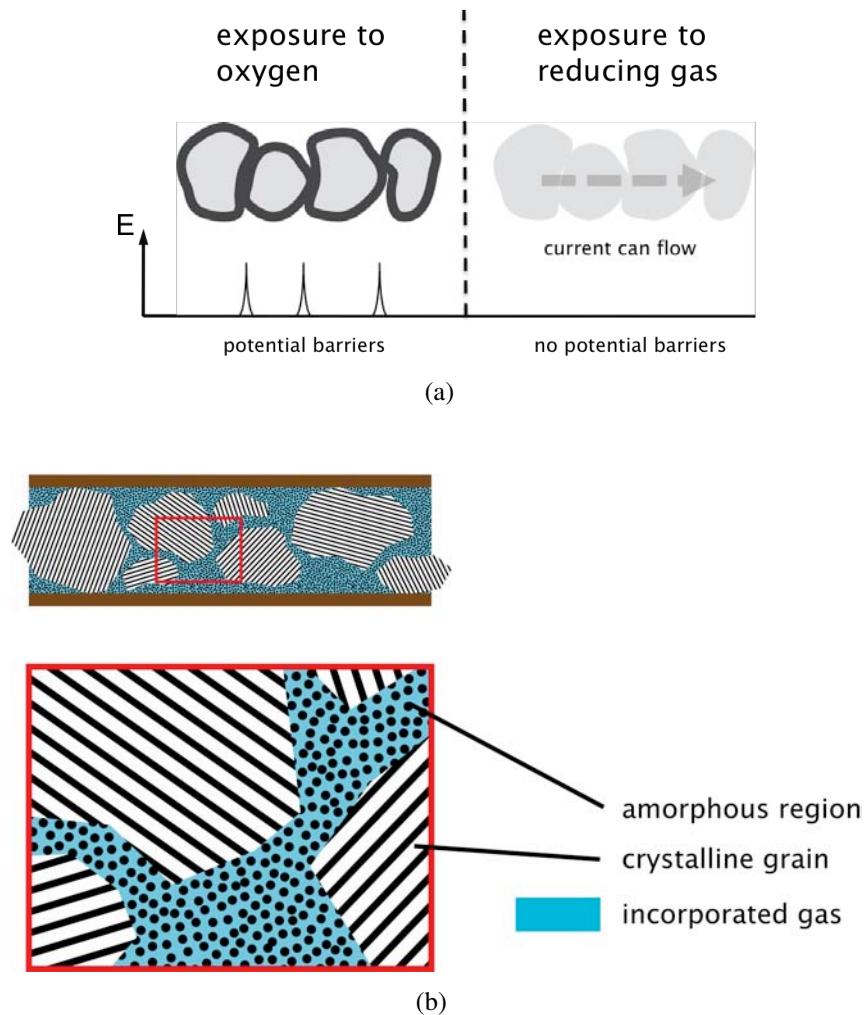


Figure 6.4: Schematic illustrations of grain boundary barriers. In (a) exposure to oxygen results in depletion of charge carriers in the surface-near regions resulting in an increase of the resistance. Exposure to reducing agents instead removes the adsorbed oxygen, the trapped electrons are released and introduced into the conduction band again. The resistance decreased. In (b) a part of a nanowire with grains embedded into amorphous or porous material is shown. The ambient gas (indicated by the blue color) is incorporated into the finely-grained core of the nanowire thereby changing the resistance of current paths between single crystallites.

adsorption may also occur in the whole volume accessible. This multiply enhances the change in conductivity offering an improved sensing capability.

Due to the finely grained crystallites observed by TEM showing diameters in the order of about 25 nm one could assume that the sensing potential of these nanowire sensors result from the change of the conductance due to reduced grain boundary barriers [52, 54]. This process is schematically shown in the illustrations in Fig. 6.4. In Fig. 6.4(a) the influence of gases such as oxygen is compared to reducing gases. Adsorption of oxygen results in a depletion of charge carriers due to electron trapping. The resistance at the grain boundaries is increased. With reducing gases instead these electrons are released which results in a decrease of the resistance. In (b) the recrystallized Sb grains are embedded in amorphous texture. By absorption of gas into the amorphous and maybe porous regions the resistance of the paths connecting the grains is changed.

With this mechanism, sensor materials allowing high sensitive measurement in the ppm range can be explained. Even smallest amounts of ambient gas incorporated into the sensor volume should result in significant change of the conducting behavior if showing interaction with the sensitive layer. A kind of saturation of the sensor volume at a certain gas pressure should lead to constant resistance unmodified with further introduction of gas. Therefore, even small amounts of gas should result in a strong increase of conductivity at very low concentrations. As the saturation level is reached no further information about the actual concentration is provided, thereby giving only a lower bound for the gas concentration. However, the sensor characteristic of the Sb nanowire exposed to water and ethanol, which shows a strong increase of the sensitivity at high pressures of the gas to be detected, is in contradiction to the grain boundary barrier mechanism. This is very sensitive at low concentration but once the substrate surface is saturated, no more change in the conductivity can be observed. Therefore this kind of mechanism can be ruled out.

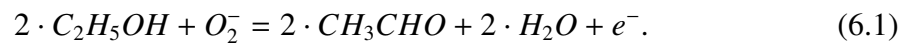
## 6.2.2 Modulation of Charge Carrier Concentration

In case of exposure of a metal oxide based sensor to atmospheric gases, chemisorption of the ambient gases takes place. Surface reactions lead to change of the overall conductance

of the sensitive layer. Oxygen ionosorption in molecular ( $O_2^-$ ) and atomic ( $O^-$ ,  $O^{--}$ ) form due to electron affinity of adsorbed oxygen results in the formation of a depletion layer at the sensor surface. This increases the electrical resistance of the surface. In contrast to that, reducing gases such as CO react with the surface oxygen ions. By removing the negatively charged oxygen the before trapped electrons are released into the conduction band resulting in a decrease of surface resistance.

Whereas water molecules are adsorbed by physisorption or hydrogen bonding, hydroxyl appears due to separation of  $H_2O$  into a negatively charged  $OH^-$  leaving a hydrogen atom ready for reaction with prior adsorbed oxygen or oxygen provided by the sensor material. For  $SnO_2$  the increase of the surface conductivity is experimentally proven. The authors in [6] present as possible mechanisms two direct processes proposed by Heiland and Kohl and a third, indirect by Morrison and by Henrich and Cox. Each of these mechanisms leads to the injection of at least one electron in the conduction band increasing the surface conductivity compared to the initial state. Whether this electron is free due displacement of before adsorbed oxygen or generated in a reaction between dissociated water and the lattice oxygen is still unexplained.

However, to use this model as an explanation for nanowire sensors, a schematic is displayed in Fig. 6.5. The sensitive surface (in this case surrounding the nanowire surface) is covered by a chemisorbed layer of the molecules which are present in a vapor phase in the ambient. Ionosorption of this gas on the metal oxide based sensor surface results the change of the charge carrier concentration in the conduction band [53]. In case of exposure of the sensor to air, oxygen molecules are adsorbed on the nanowire surface. These molecules capture electrons from the conduction layer, which results in a higher resistance of the sensor material. As already mentioned, nanowire sensors exposed to reducing gases instead, e.g. CO or ethanol gas, results in lowering of the resistance as molecules react with oxygen ions on the surface of the nanowire. For ethanol this reaction is according to the equation



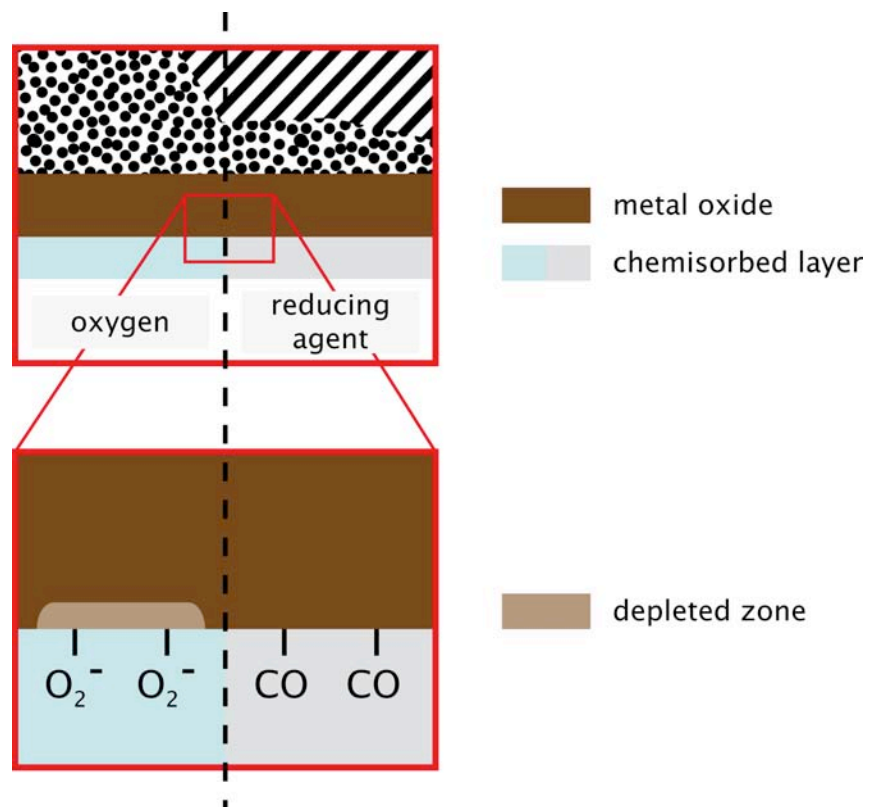


Figure 6.5: Chemisorption of gas molecules on the sensor surface. With oxygen adsorption electrons from the conduction band are trapped resulting in an increase of the resistivity of the metal oxide layer. With exposure to reducing gases such as CO these electrons can be released into conduction band again.

Due to several reasons this model cannot describe the phenomena observed with the Sb nanowire sensors. First of all, the conductivity in vacuum should increase compared to that in air, as the oxygen desorbs. This effect is not observed. Secondly, one would expect a decrease of the sensitivity at higher gas pressures, as the sensing mechanism should be caused by the first monolayer of adsorbed gas. In case of detection of water vapor this is already obtained at 20% of the vapor pressure [55, 56]. The exponential increase of the sensitivity is in contradiction to that. And finally, the sensor exposed to CO should also show reduced resistance, as these molecules react with the oxygen on the nanowire surface. No change of the electrical behavior is observed with introduction of CO instead of O<sub>2</sub> [4, 5, 6].

### 6.2.3 Conduction by Grottuss Proton Transfer Mechanism

If there is no conduction through the sensitive matter or on the surface, the only possibility left is conduction through an adsorbed film of gas molecules. It is reported that the impact of water vapor on the conductivity of MnWO<sub>4</sub> thick-film layers is affected by the stage of adsorption. The whole adsorption process can mainly be divided in a chemisorption dominated process at lower humidity and a physisorption process following at higher water concentration. At low humidity the water vapor adsorbed on the surface is dissociated forming hydroxyl ions. At a relative humidity of 20% approximately one monolayer of water completely covers the surface [55, 56]. With increasing humidity further layers of water molecules are physically adsorbed on this chemisorbed layer. The observed increase of conductivity is explained by the so called Grottuss proton transfer. The formation of hydronium (H<sub>3</sub>O<sup>+</sup>) as a combination of the free hydrogen ion generated in the chemisorption step and the physisorbed water molecules results in an increase in protonic conductivity. At even higher humidity, the ongoing increase of conductivity can be explained by condensation of water molecules and electrolytic conduction. In Tab. 6.1 the dominant charge carriers for the reported MnWO<sub>4</sub> layers at different adsorption stages are specified.

To illustrate this mechanism a schematic is shown in Fig. 6.6. In an early adsorption stage (a) chemisorption leads to ionic conduction with H<sup>+</sup> as charge carriers hop-



Adsorption stage	Conduction type	Transport mechanism
Without water	Electric	$\text{Mn}_2^+ + \text{Mn}_3^+ = \text{Mn}_3^+ + \text{Mn}_2^+$
Chemisorption	Ionic	$\text{H}^+$ - hopping on surface
Physisorption	Ionic	$\text{H}^+$ - transfer between adjacent $\text{H}_2\text{O}$ molecules
Condensation	Electrolytic	$\text{H}^+$ - transfer between positive and negative electrode

Table 6.1: Transport mechanism with  $\text{MnWO}_4$  layers as a function of water coverage [57].

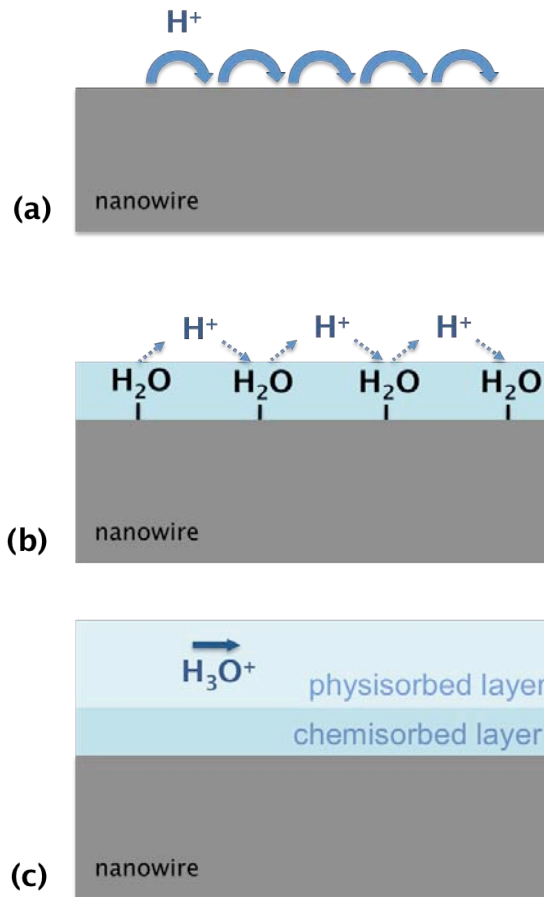


Figure 6.6: Schematic illustration of the different transport mechanisms depending on the stage of water adsorption. At low humidity (a) chemisorption generates  $\text{H}^+$ . The ionic conduction takes place by hopping of these free charge carriers on the surface. With further adsorption (b) adjacent  $\text{H}_2\text{O}$  molecules enable the proton transfer. At high humidities (c) conductivity is dominated by an electrolytic mechanism in a condensed water film.

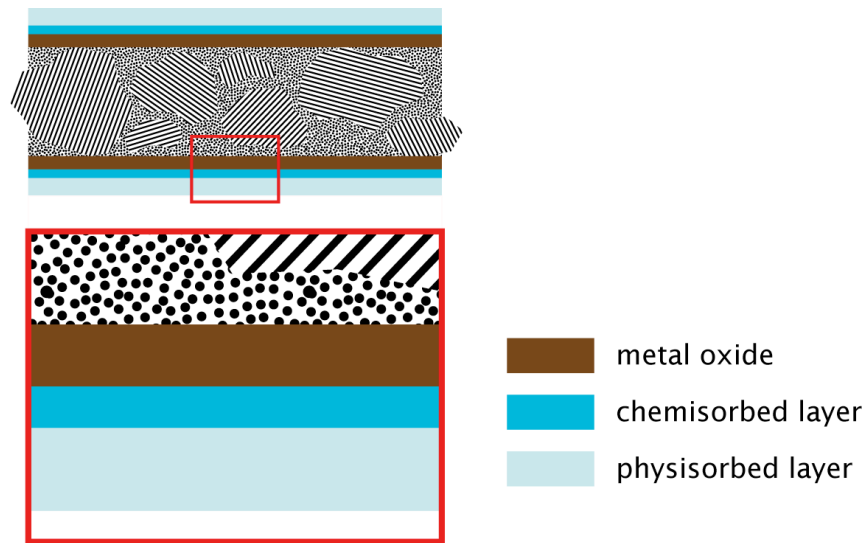


Figure 6.7: The initial nanowire surrounded by an oxide layer is first covered by a chemisorbed layer of gas molecules generating ionic charge carriers by dissociation. Further physisorption of additional gas molecules builds up a film that may act as medium for electrolytic conduction.

ping on the surface. Further adsorption (b) results in a physisorbed layer supporting the  $H^+$  transfer between adjacent  $H_2O$  molecules. Finally condensation (c) leads to electrolytic conduction, the charge carrier transfer occurs in the condensed film. For the nanowire sensor device Fig. 6.7 shows the different layers involved into the sensing process. A chemisorbed layer is covered by further physisorbed layers of gas molecules. The nanowire material (especially the outer shell) might act as a kind of preferential site for chemisorption and physisorption of the ambient gas, respectively. The conduction does not occur in the nanowire itself, the current flows through the physisorbed film. The more gas molecules are physisorbed and hence the thickness of the film supporting conductance increases, the lower is the measured resistivity providing information of the ambient, both, kind of gas and current pressure. Nevertheless, the Sb nanowires must somehow provide specific sites enhancing to chemisorption and dissociation of water and ethanol.

To our present knowledge, this model to describe the sensing mechanism seems to be most reasonable. It states chemisorption of the gas molecules on the sensor material surface by a dissociation mechanism, which in case of water forms hydroxyl ions on the surface followed by further physically adsorption of water molecules at increasing hu-

midity [55, 57]. The electrical conductivity can be illustrated by a charge carrier transport through the condensed water film as given in Fig. 6.7.

That the suggestion of this mechanism to explain the sensing properties of our Sb nanowires might be right is further emphasized as  $\text{MnWO}_4$  layers reported in [57] show very similar characteristic when exposed to water vapor. Impact on the conductivity is observed starting at partial pressures comparable to 30% relative humidity significant increasing as further water vapor is introduced. The operating temperature for this measurements is - as for our device - room temperature and the observed change in conductivity goes over 3 orders of magnitude and that might be another indication that the sensing properties can be described by chemisorption and physisorption of water and ionic conductance in the water film and analogue processes with presence of ethanol vapor instead.

## 6.3 Further Criteria for Consideration

### Time Dependency of Response and Recovery

The sensing mechanism explained by physisorption of ambient gas molecules on a prior chemisorbed layer is also reported for various sensor materials. Additional investigation and analysis concerning time dependency of the sensing process might be interpreted as a further indication that the general sensing effect is the same for Sb nanowires (covered by a thin oxide layer) and for  $\text{SnO}_2$ ,  $\text{MnWO}_4$  and some other metal oxide semiconductor materials still under investigation.

### Impact of Sb Nanowire Temperature

Another thing worth being mentioned is the ethanol sensing capability of  $\text{Sb}_2\text{O}_3$  layers deposited on oxides is reported [61, 60]. The operating temperature for these device is 400 to 600 °C and the investigation has been carried out for ethanol concentrations ranging from 1 to 100 ppm. Of course, the sensing mechanism of a 2D layer at these low concentrations has to be seen from a different angle as our nanowire sensor device

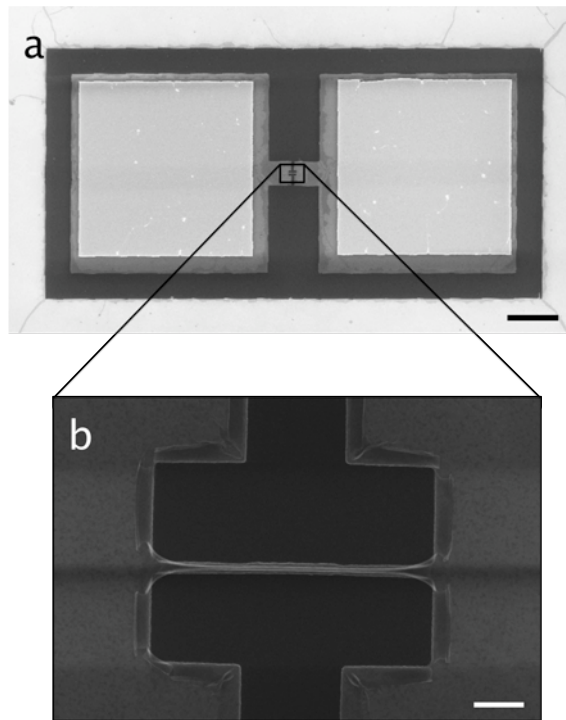


Figure 6.8: SEM images of Sb nanowire structures processed in a top-down approach. In (a) a general view of the Sb nanowire device is shown (scale bar,  $20\ \mu\text{m}$ ). A close-up view in (b) shows the actual Sb nanowire with a length of  $3\ \mu\text{m}$ , a width below  $100\ \text{nm}$  and a thickness of  $30\ \text{nm}$ . Scale bar,  $500\ \text{nm}$ .

with a much smaller sensitive surface and investigation at pressures far beyond the ppm level. Even though showing maximum sensitivities of only 1,5 approximately, at least a response to reducing gases has been evaluated in this investigation.

### **Investigation of Alternatively Processed Sb Nanostructures**

Finally top-down processed Sb nanostructures as shown in Fig. 6.8 were investigated. The pattern was 3  $\mu\text{m}$  long, about 100 nm wide and 30 nm thick. The I/V characteristic showed metallic conduction behavior. Thermal treatment at 300 °C for 30 min at air should result in a coverage of the Sb nanowire by an oxide layer. Following measurements did not shown any metallic conduction behavior of these nanostructures anymore. Exposure to water vapor (by breathing at the device) resulted in an increase of conductivity, although not that impressive as observed with the FIB generated Sb nanowires. By that reason, the supposed oxide layer covering the nanowire in combination with the ambient atmosphere seem to be essential for the electrical properties of the nanostructure and therefore for the sensing capabilities.

## Chapter 7

### Summary and Outlook

Starting with a short introduction on nanowires, different growth mechanisms and some aspects concerning their potential capabilities in Chapter 1, an overview on FIB processing especially concerning the setup and the scanning strategy is given in Chapter 2. The FIB response to several materials is described in more detail in Chapter 3. Chapter 4 has its focus on FIB induced synthesis and analysis of Sb nanowires, trying to explain the observed phenomena of nanowire formation. In Chapter 5 electrical characterization of single Sb nanowires is shown, giving information on their conducting behavior under atmospheric condition, in vacuum and with introduction of several gases. The response of the Sb nanowire device to water vapor and ethanol vapor is discussed in Chapter 6, trying to find out the actual sensing mechanism leading to variation in conductance of 4 orders of magnitude.

We presented the formation of nanopatterns as a result of the incidence of a focused ion beam onto various substrates. Interaction between accelerated ions and substrate atoms and an evolution of the surface takes place, when a sample surface is exposed to a FIB. Depending on substrate material and FIB parameters such as ion energy and ion fluence several interesting effects could be observed. With GaAs exposed to the FIB decomposition, selective etching and the agglomeration of Ga to liquid droplets on the surface was observed. FIB exposure of InAs leads to the formation of crystalline microprotrusions, due to an excess of mobile In species on the surface.

The formation of 1D nanostructures in form of nanowires was observed for substrates such as Ge, GaSb and Sb. Nanowires with lengths up to several  $\mu\text{m}$  and diameters of some tens of nm were generated due to the impact of a focused ion beam. In case of Sb the as-grown nanowires are amorphous with remarkable uniform diameters in the range of about 25 nm along their entire length. The nanowires are generated even on places not directly irradiated by the FIB. The synthesis of these nanowires is suggested to base on a catalytic process related to the VLS growth mechanism necessitating a catalytic particle, mostly a eutectic alloy, with a low melting point.

FIB induced generation of In nanowires on an In-rich InGaN layer with a thickness of 300 nm has been reported recently [62]. Single crystalline nanowires with lengths up to 30  $\mu\text{m}$  and diameters in the range of 50 – 200 nm were observed. According to the authors suggestion, exposure of InGaN to the FIB should lead to phase decomposition breaking the weaker bond between In and N. In might diffuse through the surface layer and precipitates as nanowire. Electron energy loss spectroscopy (EELS) proved the composition of the InGaN layer after FIB irradiation to consist mostly of Ga and N as the In was needed for the formation of the nanowire. The authors assumed a growth at the bottom of the wire at the interface to the substrate, fed by the In from the substrate. This report indicates that FIB induced nanowire growth is not solely limited to materials investigated in this thesis (Ge, GaSb and Sb). There are some more (mainly compound) materials with convenient properties (especially concerning melting temperature and thermal conduction).

It is further shown, that the scanning strategy had a great impact on the resulting appearance of the nanofiber network. Multi pass scanning leads to nanowire growth only outside the milling area as nanowire growth inside the milling area is eliminated by the periodic return of the FIB. The irradiated boxes processed in single pass mode were properly overgrown by Sb nanowires. The formation of a ramp-like structure as a result of the pixel-by-pixel and accordingly of the line-by-line scanning strategy was observed and discussed. The suggested mechanism was proved by FIB milling under oblique angles leading to an increase or decrease of the uplifting effect due to the variation of the escape angles for sputtered Sb clusters.

Detailed investigation of the morphological structure and the chemical composition of individual Sb nanowires was done. TEM analysis showed, that the as-grown Sb nanowires were completely amorphous, EDX analysis and Raman spectroscopy further proved the nanowire to consist of nearly pure Sb most probably surrounded by a thin oxide shell.

Annealing of the nanowires at temperatures even below 200 °C yielded in the formation of crystalline grains with diameters in the range of the nanowire diameter embedded in the amorphous nanowire material. Diameter and shape of the nanowire remained unaffected by the annealing process.

Individual nanowires transferred onto isolating substrate surfaces were contacted by means of EBL processing Ti/Au pads for electrical characterization. It was observed, that the water vapor content in the ambient atmosphere showed a great impact on the measurement. The results of investigation under atmospheric conditions were compared to those gained in vacuum and by introduction of several gases. No influence on the conductivity was observed with introduction of He, H<sub>2</sub>, O<sub>2</sub> and - surprisingly - CO. In contrast to that resistance of the single Sb nanowire changed significantly when exposed to water or ethanol vapor.

Intense literature survey yielded a few possible sensing mechanisms to describe the observed phenomena. The most probably explanation for the sensing capability of Sb nanowires deals with chemisorption and physisorption of ambient gas molecules providing both, charge carriers and medium for the conduction. Additionally we did investigation of response and recovery time, as this parameter is of great interest for practicable use of Sb nanowires as sensors.

Based on the results reported in this thesis investigation of further gases in particular reducing agents would be interesting. Another interesting aspect in regard to a future application is the chemical stability. Reactive species, such as chlorides, might have negative effects on the durability of the Sb nanowire, this still has to be proved.

So far, the processed Sb nanowire devices were tested on response to gases such as He, H<sub>2</sub>, CO and O<sub>2</sub> resulting in no change of resistivity of the nanowire and water and ethanol



---

vapor showing a significant change in conductivity. Depending on kind and amount of introduced gas changes of the nanowire resistivity up to 4 orders of magnitude compared to the initial nanowire resistance in vacuum is observed.

## Bibliography

- [1] Y Cui and C M Lieber. Functional nanoscale electronic devices assembled using silicon nanowire building blocks. *Science*, 291:851, 2001.
- [2] Y Huang, X Duan, and C M Lieber. Nanowires for integrated multicolor nanophotonics. *Small*, 1(1):142, 2005.
- [3] Y Cui, Q Wei, H Park, and C M Lieber. Nanowire nanosensors for highly sensitive and selective detection of biological and chemical species. *Science*, 293:1289, 2001.
- [4] A Gurlo. Interplay between  $\text{O}_2$  and  $\text{SnO}_2$ : Oxygen ionosorption and spectroscopic evidence for adsorbed oxygen. *ChemPhysChem*, 7(10):2041, 2006.
- [5] A Gurlo and Riedel R. In situ and operando spectroscopy for assessing mechanisms of gas sensing. *Angew. Chem. Int. Ed.*, 46(21):3826, 2007.
- [6] N Barsan and U Weimar. Understanding the fundamental principles of metal oxide based gas sensors; the example of CO sensing with  $\text{SnO}_2$  sensors in the presence of humidity. *J. Phys.: Condens. Matter*, 15(20), 2003.
- [7] F Hernandez-Ramirez, S Barth, A Tarancon, O Casals, J Pellicer, E Rodriguez, A Romano-Rodriguez, J R Morante, and S Mathur. Water vapor detection with individual tin oxide nanowires. *Nanotechnology*, 18(42):424016, 2007.
- [8] Y Zhang, A Kolmakov, S Chretien, H Metiu, and M Moskovits. Control of catalytic reactions at the surface of a metal oxide nanowire by manipulating electron density inside it. *Nano Lett.*, 4(3):403, 2004.

- 
- [9] P-C Chang, H-Y Chen, J-S Ye, F-S Sheu, and J G Lu. Vertically aligned antimony nanowires as solid-state pH sensors. *ChemPhysChem*, 8(1):57, 2007.
- [10] A Star, J-P Gabriel, K Bradley, and G Gruner. Electronic detection of specific protein binding using nanotube fet devices. *Nano Lett.*, 3(4):459, 2003.
- [11] J R Health and F K LeGoues. A liquid solution synthesis of single crystal germanium quantum wires. *Chem. Phys. Lett.*, 208(3-4):263, 1993.
- [12] J Westwater, D P Gosain, S Tomiya, S Usui, and H Ruda. Growth of silicon nanowires via gold/silane vapor-liquid-solid reaction. *J. Vac. Sci. Technol. B*, 15(3):554, 1997.
- [13] R Martel, T Schmidt, and H Shea. Single- and multi-wall carbon nanotube field-effect transistors. *Appl. Phys. Lett.*, 73(17):2447, 1998.
- [14] Y Xia, P Yang, Y Sun, Y Wu, B Mayer, Y Gates, B and Yin, F Kim, and H Yan. One-dimensional nanostructures: Synthesis, characterization, and applications. *Adv. Mater.*, 15(5):353, 2003.
- [15] J D Holmes, K P Johnstone, R C Doty, and B A Korgel. Control of thickness and orientation of solution-grown silicon nanowires. *Science*, 287:1471, 2000.
- [16] H Jiantao, W O Teri, and C M Lieber. Chemistry and physics in one dimension: Synthesis and properties of nanowires and nanotubes. *Acc. Chem. Res.*, 32(5):435, 1999.
- [17] Y Cui, L J Lauhon, M S Gudiksen, J Wang, and C M Lieber. Diameter-controlled synthesis of single-crystal silicon nanowires. *Appl. Phys. Lett.*, 78(15):2214, 2001.
- [18] A Lugstein, M Steinmair, Y J Hyun, E Bertagnolli, and P Pongratz. Ga/Au alloy catalyst for single crystal silicon-nanowire epitaxy. *Appl. Phys. Lett.*, 90(2):023109, 2007.
- [19] C Schoendorfer, A Lugstein, L Bischoff, Y J Hyun, P Pongratz, and E Bertagnolli. FIB induced growth of antimony nanowires. *Microelectron. Eng.*, 84(5-8):1440, 2007.

- 
- [20] C Schoendorfer, A Lugstein, L Bischoff, P M Nellen, V Callegari, Y J Hyun, P Pongratz, and E Bertagnolli. Focused ion beam induced synthesis of a porous antimony nanowires network. *J. Appl. Phys.*, 102(4):044308, 2007.
- [21] E Chason, T M Mayer, B K Kellerman, D T McIlroy, and A J Howard. Roughening instability and evolution of the Ge(001) surface during ion sputtering. *Phys. Rev. Lett.*, 72(19):3040, 1994.
- [22] G Carter and V Vishnyakov. Roughening and ripple instabilities on ion-bombarded Si. *Phys. Rev. B*, 54(24):17647, 1996.
- [23] Z X Jiang and P F A Alkemade. The complex formation of ripples during depth profiling of Si with low energy, grazing oxygen beams. *Appl. Phys. Lett.*, 73(3):315, 1998.
- [24] J Erlebacher, M J Aziz, E Chason, M B Sinclair, and J A Floro. Spontaneous pattern formation on ion bombarded Si(001). *Phys. Rev. Lett.*, 82(11):2330, 1999.
- [25] S Rusponi, C Boragno, and U Valbusa. Ripple structure on Ag(110) surface induced by ion sputtering. *Phys. Rev. Lett.*, 78(14):2795, 1999.
- [26] S Rusponi, G Costantini, C Boragno, and Valbusa U. Scaling laws of the ripple morphology on Cu(110). *Phys. Rev. Lett.*, 81(19):4184, 1998.
- [27] T M Mayer, E Chason, and Howard A J. Roughening instability and ion-induced viscous relaxation of SiO<sub>2</sub> surfaces. *J. Appl. Phys.*, 76(3):1633, 1994.
- [28] S Habenicht, W Bolse, K P Lieb, K Reimann, and U Geyer. Nanometer ripple formation and self-affine roughening of ion-beam-eroded graphite surfaces. *Phys. Rev. B*, 60(4), 1999.
- [29] J Melngailis. Focused ion beam technology and applications. *J. Vac. Sci. Technol. B*, 5(2):469, 1987.
- [30] J Suhua, N Jingfeng, and W Jiaji. Investigation on properties of focused ion beam enhanced etching. *6th International Conference On Solid-State And Integrated-Circuit Technology Proceedings*, 2:1091, 2001.

- [31] J G Pellerin, D P Griffis, and P E Russell. Focused ion beam machining of Si, GaAs, and InP. *J. Vac. Sci. Technol. B*, 8(6):1945, 1990.
- [32] A Lugstein, M Weil, B Basnar, C Tomastik, and E Bertagnolli. A novel fabrication technique for crystallite growth on a (100) InAs surface utilizing focused ion beams. *Nucl. Instr. and Meth. in Phys. Res. B*, 222(1-2):91, 2004.
- [33] A Lugstein, B Basnar, W Brezna, M Weil, S Golka, and E Bertagnolli. Advanced nanopattern formation by a subtractive self-organization process with focused ion beams. *Nucl. Instr. and Meth. in Phys. Res. B*, 242(1-2):93, 2006.
- [34] International Centre for Diffraction Data. *The Powder Diffraction File*. 12 Campus Boulevard, Newton Square, PA 19073-3273, USA.
- [35] N Nitta, M Taniwaki, Y Hayashi, and T Yoshiie. Formation of cellular defect structure on GaSb ion-implanted at low temperature. *J. Appl. Phys.*, 92(4):1799, 2002.
- [36] S Lipp, L Frey, C Lehrer, B Frank, E Demm, and H Ryssel. Investigations on the topology of structures milled and etched by focused ion beams. *J. Vac. Sci. Technol. B*, 14(6):3996, 1996.
- [37] R S Wagner and W C Ellis. Vapor-liquid-solid mechanism of single crystal growth. *Appl. Phys. Lett.*, 4(5):1799, 1964.
- [38] E I Givargizov. Fundamental aspects of VLS growth. *J. Cryst. Growth*, 31:20, 1975.
- [39] A M Morales and C M Lieber. A laser ablation method for the synthesis of crystalline semiconductor nanowires. *Science*, 279:208, 1998.
- [40] Y Wang, V Schmidt, S Senz, and U Gösele. Epitaxial growth of silicon nanowires using an aluminium catalyst. *Nature Nanotechnology*, 1:186, 2006.
- [41] T I Kamins, R S Williams, D P Basile, and Harris J S. Ti-catalyzed Si nanowires by chemical vapor deposition: Microscopy and growth mechanisms. *J. Appl. Phys.*, 89(2):1008, 2001.
- [42] M K Sunkara, S Sharma, R Miranda, G Lian, and E C Dickey. Bulk synthesis of silicon nanowires using a low-temperature vaporliquid-solid method. *Appl. Phys. Lett.*, 79(10):1546, 2001.

- [43] Z W Pan, Z R Dai, C Ma, and Z L Wang. Molten gallium as a catalyst for the large-scale growth of highly aligned silica nanowires. *J. Am. Chem. Soc.*, 124(8):1817, 2002.
- [44] B Predel. *Landolt-Börnstein - Group IV Physical Chemistry, Ga-Gd - Hf-Zr*. Springer-Verlag, 1996.
- [45] M Barati, J C L Chow, P K Ummat, and W R Datars. Temperature dependence of the resistance of antimony nanowire arrays. *J. Phys.: Condens. Matter*, 13(13):2955, 2001.
- [46] C S Barrett, P Cucka, and K Haefner. The crystal structure of antimony at 4.2, 78 and 298 K. *Acta Cryst.*, 16:451, 1963.
- [47] D K Schroder. *Semiconductor Material and Device Characterization*. John Wiley & Sons, 1998.
- [48] D R Lide. *CRC Handbook of Chemistry and Physics, A Ready-Reference Book of Chemical and Physical Data*. CRC Press LLC, 1997.
- [49] W Göpel and K D Schierbaum. SnO<sub>2</sub> sensors: current status and future prospects. *Sens. Actuators B*, 26(1-3):1, 1995.
- [50] N Barsan and U Weimar. Conduction model of metal oxide gas sensors. *J. Electroceram.*, 7(3):143, 2001.
- [51] D Zhang, Z Liu, C Li, T Tang, X Liu, S Han, B Lei, and C Zhou. Detection of NO<sub>2</sub> down to ppb levels using individual and multiple In<sub>2</sub>O<sub>3</sub> nanowire devices. *Nano Lett.*, 4(10):1919, 2004.
- [52] P Feng, X Y Xue, Y G Liu, and T H Wang. Highly sensitive ethanol sensors based on {100}-bounded In<sub>2</sub>O<sub>3</sub> nanocrystals due to face contact. *Appl. Phys. Lett.*, 89(24):243514, 2006.
- [53] X Y Xue, Y J Chen, Y G Wang, and T H Wang. Synthesis and ethanol sensing properties of ZnSnO<sub>3</sub> nanowires. *Appl. Phys. Lett.*, 86(23):233101, 2005.

- 
- [54] X Y Xue, P Feng, Y G Wang, and Wang T H. Extremely high oxygen sensing of individual  $\text{ZnSnO}_3$  nanowires arising from grain boundary barrier modulation. *Appl. Phys. Lett.*, 91(2):022111, 2007.
- [55] X Q Fu, C Wang, H C Yu, Y G Wang, and T H Wang. Fast humidity sensors based on  $\text{CeO}_2$  nanowires. *Nanotechnology*, 18(14):145503, 2007.
- [56] W Qu and W Wlodarski. A thin-film sensing element for ozone, humidity and temperature. *Sens. Actuators B*, 64(1-3):42, 2000.
- [57] W Qu and J-U Meyer. Thick-film humidity sensor based on porous  $\text{MnWO}_4$  material. *Meas. Sci. Technol.*, 8(6):593, 1997.
- [58] M Li and Y Chen. An investigation of response time of  $\text{TiO}_2$  thin-film oxygen sensors. *Sens. Actuators B*, 32(1):83, 1996.
- [59] M L Zhang, Z H Yuan, and C Zheng. Fast response of undoped and Li-doped titania thick-films at low temperature. *Sens. Actuators B*, 131(2):680, 2008.
- [60] R Binions, C J Carmalt, and I P Parkin. A comparison of the gas sensing properties of solid state metal oxide semiconductor gas sensors produced by atmospheric pressure chemical vapour deposition and screen printing. *Meas. Sci. Technol.*, 18(1):190, 2007.
- [61] R Binions, C J Carmalt, and I P Parkin. Antimony oxide thin films from the atmospheric pressure chemical vapour deposition reaction of antimony pentachloride and ethyl acetate. *Polyhedron*, 25(15):3032, 2006.
- [62] S S Oh, D H Kim, M-W Moon, A Vaziri, M Kim, E Yoon, K H Oh, and J W Hutchinson. Indium nanowires synthesized at an ultrafast rate. *Adv. Mater.*, 20(6):1093, 2008.

## List of Own Publications

1. C. Schoendorfer, A. Lugstein, Y.-J. Hyun, E. Bertagnolli, L. Bischoff, P. M. Nellen, V. Callegari, and P. Pongratz:  
*Focused ion beam induced synthesis of a porous antimony nanowire network*  
J. Appl. Phys. 102, 044308 (2007).
2. C. Schoendorfer, A. Lugstein, L. Bischoff, Y.J. Hyun, P. Pongratz and E. Bertagnolli:  
*FIB induced growth of antimony nanowires*  
Microelectron. Eng. 84, 1440 (2007).
3. A. Lugstein, C. Schoendorfer, M. Weil, C. Tomastik, A. Jauss, E. Bertagnolli:  
*Study of focused ion beam response of GaSb*  
Nucl. Instrum. Methods Phys. Res., Sect. B 255, 309 (2007).
4. C. Schoendorfer, A. Lugstein, E. Bertagnolli:  
*Focused Ion Beam induced Nanodot and Nanofiber Growth*  
Microelectron. Eng. 83, 1491 (2006).



## List of Own Conference Contributions

1. MRS Spring Meeting, San Francisco, USA; 03/24/2008 - 03/28/2008  
*Antimony Nanowires as Chemical Sensors* (Talk)
2. International Conference on Micro- and Nano-Engineering 2007, Copenhagen, Denmark; 09/23/2006 - 09/26/2006 (Poster presentation)
3. MRS Fall Meeting, Boston, USA; 11/27/2006 - 12/01/2006  
*Focused Ion Beam Induced Growth of Antimony Nanowires* (Talk)
4. GMe Workshop 2006, Vienna, Austria; 10/13/2006 (Poster presentation)
5. International Conference on Micro- and Nano-Engineering 2006, Barcelona, Spain; 09/17/2006 - 09/20/2006 (Poster presentation)
6. International Conference on Physics of Semiconductor (ICPS-28), Vienna, Austria; 07/24/2006 - 07/28/2006 (Poster presentation)
7. 55th Annual Meeting of the Austrian Physical Society, Vienna, Austria; 09/27/2005 - 09/25/2005  
*Focused Ion Beam assisted Formation of Nanostructures* (Talk)

- 
8. International Conference on Micro- and Nano-Engineering, Vienna, Austria;  
09/19/2005 - 09/22/2005 (Poster presentation)

# Curriculum Vitae

## Dipl.-Ing. Christoph Schöndorfer

Geburtsdatum: 18. April 1977

Geburtsort: Schärding

Nationalität: Österreich

Familienstand: ledig

## Ausbildung

09/04 - 06/08 Doktoratsstudium an der TU Wien

Dissertation am Institut für Festkörperelektronik

Thema: *Focused Ion Beam induced Synthesis of Nanowires*

10/96 - 04/04 Studium der Technischen Physik an der TU Wien

Diplomarbeit am Institut für Festkörperphysik

Thema: *TEM-Untersuchung von gesputterten CoPd-Schichten  
für magnetische Datenspeicher mit höchster Dichte*

04/04 Diplomprüfung

09/87 - 06/95 BRG Schärding

06/95 Reifeprüfung

09/83 - 07/87 Volksschule Brunnenthal